

# Optimal structured light waves generation in 3D volumes using communication mode optics

Vinicius S. de Angelis<sup>1,2</sup>, Ahmed H. Dorrah<sup>1</sup>, Leonardo A. Ambrosio<sup>2</sup>, David A. B. Miller<sup>3</sup>, and Federico Capasso<sup>1,\*</sup>

<sup>1</sup>*Harvard John A. Paulson School of Engineering and Applied Sciences, Harvard University, Cambridge, MA 02138, USA*

<sup>2</sup>*Department of Electrical and Computer Engineering, São Carlos School of Engineering, University of São Paulo, 400 Trabalhador são-carlense Ave., 13566-590, São Carlos, São Paulo, Brazil*

<sup>3</sup>*Ginzton Laboratory, Stanford University, Stanford, CA 94305, USA*

*\*Corresponding author: capasso@seas.harvard.edu*

**Achieving precise control of light intensity in 3D volumes is highly in demand in many applications in optics. Various wavefront shaping techniques have been utilized to reconstruct a target amplitude profile within a 3D space. However, these techniques are intrinsically limited by cross-talk and often rely on optimization methods to improve the reconstruction quality. We propose and experimentally demonstrate a new wavefront shaping method based on interfering the optimum orthogonal communication modes connecting a source plane and a receiving volume. These optimum modes are computed from the singular value decomposition of a coupling operator that connects each point at the source plane to another one in the receiving volume. The modes comprise a pair of source and receiving eigenfunctions, each one forming a complete orthogonal basis for their respective spaces. We utilize these modes to construct arbitrarily chosen 2D and 3D structured light waves within the output receiving volume and optically generate these waves using a spatial light modulator. Our generated intensity profiles exhibit low cross-talk, high fidelity, and high contrast. We envision our work to inspire new directions in any domain that requires controlling light intensity in 3D with high precision such as in holography, microscopy, metrology, light-matter interactions, and optical sensing.**

## 1 Introduction

Harnessing the interaction between light and matter shapes our understanding of the universe. Imaging through disorder with high spatial and temporal resolution, for instance, can teach us something new about cells and other galaxies alike. Likewise, light manipulation, storage, and detection are the foundation of photonic-based technologies that include quantum computing, communications, and sensing<sup>1-7</sup>. At the heart of these developments lies the need for tailoring the properties of incoming light in a nontrivial manner<sup>8-13</sup>. Early pursuits in structured light waves include the development of custom two-dimensional (2D) light intensity patterns at a particular transverse plane using modal bases such as Laguerre-Gauss, Hermite-Gauss and Ince-Gauss modes<sup>14-17</sup>, or by deploying iterative algorithms that solve inverse problems of light propagation, notably the Gerchberg–Saxton algorithm<sup>18</sup>. Although these methods provide control over the transverse field distribution at a given 2D plane, they lack control over the longitudinal beam profile. Tailoring the spatial and temporal properties of light over a 3D volume is a sought-after goal in many applications, including microscopy, spectroscopy, light-matter interactions, and optical sensing<sup>19,20</sup>.

A variety of wavefront shaping methods have been developed to control light’s intensity in 3D. The common approach is to discretize a target 3D light distribution into a set of independent primitives. The incident waveform required to generate this target distribution is then synthesized by superposing the diffraction patterns from all the primitives in a given transverse plane. This is the principle employed in computer-generated holograms (CGH) which are often classified based on the type of their primitive<sup>21,22</sup>. Point-cloud techniques, for instance, adopt a collection of source points, each emitting a spherical wave towards the transverse plane (CGH screen). The huge number of primitives involved in this method, however, mandates the use of look-up tables and optimization algorithms to reduce the memory consumption<sup>23</sup>. Although polygon mesh techniques involve a relatively smaller number of primitives, they require an additional process of shading and texture mapping to maintain the quality of the reconstructed holograms, which inherently increases their computation time<sup>24</sup>. Multi-plane techniques mitigate this by adopting a set of parallel planes, uniformly spaced along the propagation direction. In this case, Fresnel diffraction or angular spectrum algorithms are implemented to compute the diffraction pattern from each plane<sup>25-27</sup>. These techniques have been widely adopted for creating 3D holograms as they demand a significantly smaller number of primitives compared to point-cloud and polygon mesh techniques<sup>28,29</sup>. However, since the planes are computed independently from each other, cross-talk between

their diffraction patterns often degrades the fidelity and reconstruction quality. Inter plane cross-talk can be reduced using optimization algorithms<sup>30-34</sup> which, despite their recent advances, still involve a trade-off between their computational time and reconstruction quality.

Wavefront shaping along the optical path can alternatively be achieved via a superposition of co-propagating Bessel modes with different longitudinal wavenumbers. By harnessing the spatial beating between these modes, one can modulate not only the intensity profile<sup>35-37</sup>, but also other degrees-of-freedom of light along the propagation direction including its total angular momentum<sup>38-40</sup> and its polarization<sup>41</sup>. By assembling many of these (nominally) non-diffracting light threads (uniformly spaced from each other) over a horizontal Cartesian plane, oriented parallel to the propagation direction, one can construct 2D light sheet whose intensity profile can be controlled at-will over the horizontal plane. By stacking several of those sheets over a volume, 3D structured light waves can also be synthesized<sup>42-44</sup>. Despite the continuous depth and axial resolution afforded by this technique, it still suffers from undesired cross-talk between the projected light sheets. Additionally, the reconstructed light fields often lack intensity uniformity owing to the transverse discretization of the co-propagating light threads. Convolutional neural networks have proven effective in reducing the cross-talk and also in enhancing the intensity uniformity<sup>45</sup>. However, this solution can be computationally demanding as it grows quadratically with the number of light sheets.

Multi-plane and light sheet holography both rely on optimization algorithms to minimize cross-talk, adding computational cost. The cross-talk in both methods exists as a result of employing waveforms (or modes) which do not represent an orthogonal basis and are not optimized to the entire 3D domain where the target object is projected. In this work, we propose and experimentally demonstrate a new wavefront shaping method that synthesizes a target 3D light distribution from the optimum basis set of orthogonal communication modes computed by means of the singular value decomposition (SVD) modal optics<sup>46</sup>. First we define the 3D domain of the structured light field as a receiving space. Separated from this receiving space by a finite longitudinal distance, we also define a transverse plane as a source space in which the required incident waveform is encoded to create the target structured light field. Then by computing the SVD of a coupling operator connecting these two spaces, we establish communication modes, each one comprising a pair of eigenfunctions, one in the source space and another one in the receiving space. These communication modes constitute the optimum orthogonal channels connecting these spaces for the following reasons: both the source and receiving eigenfunctions form a complete orthogonal basis

for their respective spaces; and each receiving eigenfunction corresponds to the largest possible magnitude of wave function its associated source eigenfunction can create in the receiving space. Therefore, the structured light waves constructed by interfering these modes represent the optimal construction of any target field distribution.

Obtaining the optimum orthogonal communication channels (modes) between two spaces using SVD is a more general concept which was introduced in the optics literature in 1998<sup>46</sup> and has led to many studies in wireless communications, optical fibers and optical systems<sup>47,48</sup>. Notably, SVD modal optics has recently enabled integrated photonic processors to determine the most efficient waves to send information through arbitrary and scattering optical media<sup>49</sup> as theoretically predicted in Ref. 50. Nevertheless, while communication modes have previously been analyzed for distinct source and receiving space geometric configurations including spaces comprising two rectangular volumes<sup>51</sup>, two planar transverse apertures<sup>52,53</sup> and even between an annular aperture and an axial line<sup>54</sup>, SVD modal optics has not been applied as a wavefront shaping method to create structured light waves with long depth of field in arbitrary 3D volumes such as a set of horizontal planes, oriented parallel to the optical axis. Additionally, in contrast to point-cloud and polygon mesh techniques which are usually computationally demanding owing to the large number of primitives, our SVD method incorporates a finite set of modes and, hence, is ideal for dynamic wavefront shaping and real-time holography. This is because all the communication modes are defined over the entire source and receiving spaces and need to be computed once, and then only their relative weights need to be updated for each frame, akin to a Fourier series construction.

## 2 Wavefront shaping with communication modes

In SVD modal optics, the source and receiving spaces are mathematically viewed as Hilbert spaces ( $H_S$  and  $H_R$ ) that contain the possible source and receiving eigenfunctions,  $|\Psi_S\rangle$  and  $|\Phi_R\rangle$ , as illustrated in Fig. 1(a). The connection between these spaces is established through a coupling operator  $G_{SR}$ , which for free-space scalar waves can be described by a Green's function<sup>46</sup>:

$$G_{SR,\lambda}(\mathbf{r}_R, \mathbf{r}_S) = -\frac{1}{4\pi} \frac{\exp(ik|\mathbf{r}_R - \mathbf{r}_S|)}{|\mathbf{r}_R - \mathbf{r}_S|}, \quad (1)$$

which maps a position  $\mathbf{r}_S$  at the source space to a position  $\mathbf{r}_R$  at the receiving space for a given operating wavelength  $\lambda$ . Such a scalar Green's function will usually be sufficient for describing an electromagnetic wave of a single polarization. For cases of tight focusing or near field behavior, or to use this approach for full vector fields, a similar approach can be taken using the full dyadic



Green's function <sup>48</sup>. In Eq. (1),  $k = 2\pi/\lambda$  is the wave number and a time harmonic dependence  $\exp(-i\omega_0 t)$  is assumed, with  $\omega_0 = kc$  being the operating angular frequency and  $c$  the light speed in free space. Following Ref. 48, we presume that the source space consists of  $N_S$  source points located at positions  $\mathbf{r}_{S,j}$  ( $j = 1, \dots, N_S$ ) while the receiving space contains  $N_R$  receiving points at positions  $\mathbf{r}_{R,i}$  ( $i = 1, \dots, N_R$ ), allowing us to describe  $G_{SR}$  as a  $N_R \times N_S$  matrix:

$$g_{ij} = -\frac{1}{4\pi} \frac{\exp(ik|\mathbf{r}_{R,i} - \mathbf{r}_{S,j}|)}{|\mathbf{r}_{R,i} - \mathbf{r}_{S,j}|}. \quad (2)$$

The eigenfunctions  $|\Psi_S\rangle$  and  $|\Phi_R\rangle$  are found by solving the SVD of the coupling operator matrix  $G_{SR}$  of Eq. (2) which is equivalent to solving two eigenproblems, one associated with the operator  $G_{SR}^\dagger G_{SR}$  and another one associated with  $G_{SR} G_{SR}^\dagger$ , leading to a one-to-one (injective) relation between these eigenfunctions and allowing us to establish the concept of a communication mode: a pair of eigenfunctions, one in the source space  $|\Psi_{S,j}\rangle$  that couples to another one in the receiving space  $|\Phi_{R,j}\rangle$ , with the coupling strength of this connection given by the squared absolute value of the singular values  $s_j$  of  $G_{SR}$ , i.e.,  $|s_j|^2$  (see Supplementary Note 1). Each of these eigenfunctions is mathematically a column vector, whose elements are the amplitudes at each different point in the appropriate space. Notice that  $G_{SR}^\dagger G_{SR}$ , described by a  $N_S \times N_S$  matrix, is an operator within the source space, mapping a vector in  $H_S$  back to another vector in  $H_S$ . Similarly,  $G_{SR} G_{SR}^\dagger$  is an operator within the receiving space, mapping from  $H_R$  back into  $H_R$ , being described by a  $N_R \times N_R$  matrix. Since each of these two operators is a positive Hermitian operator, its eigenfunctions (or eigenvectors) are orthogonal and form a complete set for its Hilbert space, while its eigenvalues, given by the coupling strengths  $|s_j|^2$ , are positive real numbers. Moreover, the sets  $\{|\Psi_{S,j}\rangle\}$  and  $\{|\Phi_{R,j}\rangle\}$  constitute the optimum possible orthogonal channels connecting the two spaces in terms of magnitude of the inner product. In other words, each receiving eigenfunction  $|\Phi_{R,j}\rangle$  corresponds to the largest possible magnitude of wave function its associated source eigenfunction  $|\Psi_{S,j}\rangle$  can create at the receiving space. Note that, if the points are sufficiently dense in both spaces, this approach correctly converges towards the corresponding continuous functions and spaces, with convergence guaranteed by the Hilbert-Schmidt nature of Green's function operators for waves <sup>48</sup>. For further details about this maximization property, see Supplementary Note 1.

Given a target profile  $|\Phi_T\rangle$ , i.e., a vector of amplitudes at the receiving points, the required source function  $|\Psi_T\rangle$  (vector of amplitudes at the source points) is determined by <sup>48</sup> (see Supple-

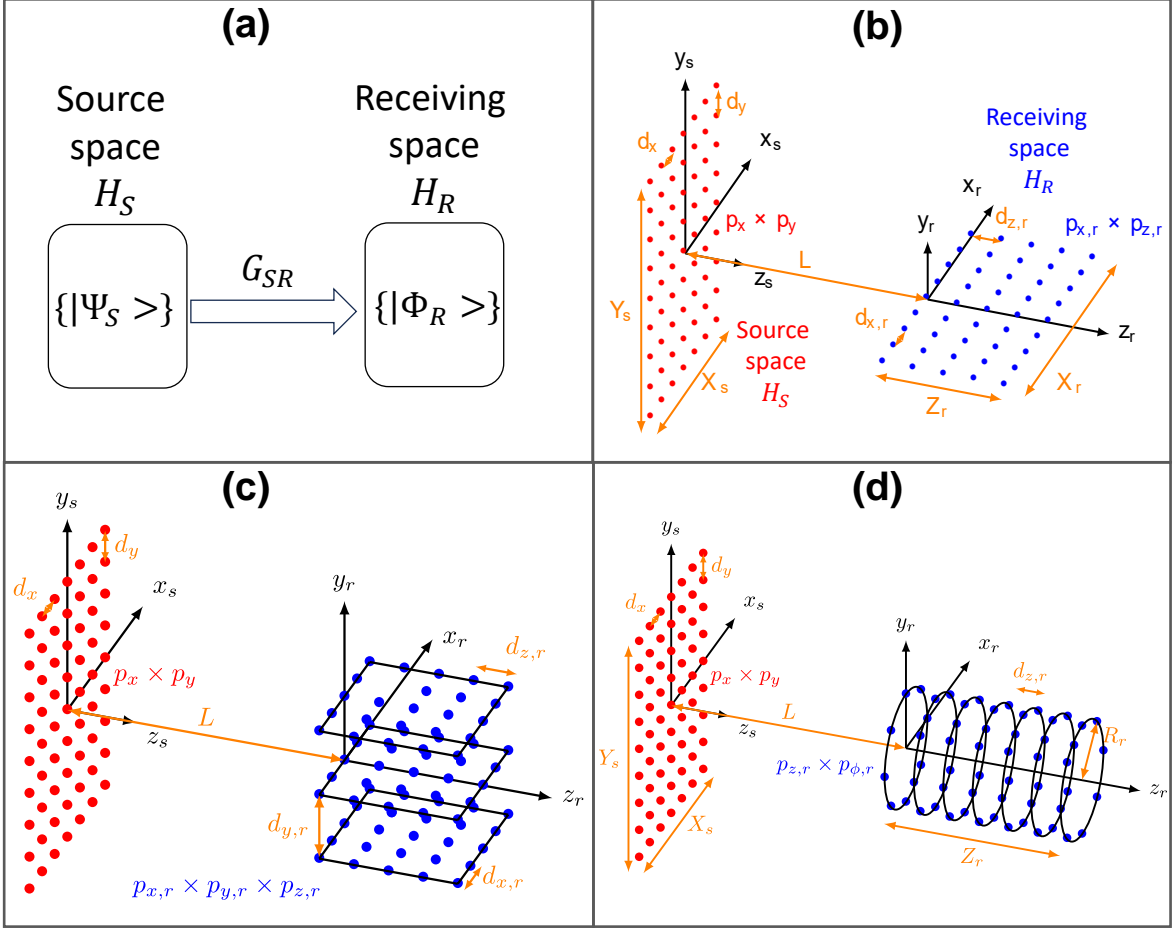


**Figure 1: General concept of communication modes and examples of source and receiving spaces.** (a) Communication modes are established through a coupling operator  $G_{SR}$  between a source and a receiving space. These spaces are mathematically viewed as Hilbert spaces ( $H_S$  and  $H_R$ ), each one containing a set of eigenfunctions ( $\{|\Psi_S\rangle\}$  and  $\{|\Phi_R\rangle\}$ ). In free space,  $G_{SR}$  is expressed by a Green's function. Assuming a collection of  $N_s$  source points and  $N_r$  receiving points to describe these spaces, we can express  $G_{SR}$  as a  $N_R \times N_S$  matrix. Examples of source and receiving space configurations in which the source points are distributed as an array of  $p_x \times p_y$  points in a transverse plane and the receiving points as an array of: (b)  $p_{x,r} \times p_{z,r}$  points in a horizontal plane, (c)  $p_{x,r} \times p_{y,r} \times p_{z,r}$  points within a set of uniformly spaced horizontal planes, and (d)  $p_{z,r} \times p_{\phi,r}$  points disposed within a set of uniformly spaced rings placed along the optical axis. In all these configurations, the spaces are separated by a distance  $L$ , an on-axis distance between their coordinate systems  $(x_s, y_s, z_s)$  and  $(x_r, y_r, z_r)$ .

mentary Note 2):

$$|\Psi_T\rangle = \sum_j \frac{1}{s_j} \langle \Phi_{R,j} | \Phi_T \rangle |\Psi_{S,j}\rangle, \quad (3)$$

in which  $\langle \Phi_{R,j} | \Phi_T \rangle$  is the projection of the target profile onto the set of receiving eigenfunctions. Because  $|\Psi_T\rangle$  is inversely proportional to the singular values  $s_j$ , in practice the summation in Eq. (3) is truncated to the first  $M$  well coupled communication modes where their coupling strengths  $|s_j|^2$  are ordered by decreasing size of their magnitude. Since the sum of these strengths is finite, bounded by a sum rule  $S$  (Supplementary Note 1), we choose a number  $M$  of modes that nearly provide  $S$ , avoiding the incorporation of modes ( $j > M$ ) with negligible  $|s_j|^2$  values. Equivalently, we can also give up adding any more terms when the resulting additional waves are so weakly coupled that we would need very large source amplitudes to generate them. The resulting wave created by the source function  $|\Psi_T\rangle$  at a position  $\mathbf{r}$  away from the source space is given by the sum of all the spherical waves emitted by the  $N_S$  source points weighted by  $|\Psi_T\rangle$ <sup>48</sup>:

$$\phi(\mathbf{r}) = -\frac{1}{4\pi} \sum_{q=1}^{N_S} \frac{\exp(ik|\mathbf{r} - \mathbf{r}_{S,q}|)}{|\mathbf{r} - \mathbf{r}_{S,q}|} h_q, \quad (4)$$

where  $h_q$  is the  $q$ -th component of  $|\Psi_T\rangle$ , such that  $|\Psi_T\rangle = [h_1 \ h_2 \ \dots \ h_{N_S}]^T$ .

Assuming Cartesian coordinate systems  $(x_s, y_s, z_s)$  and  $(x_r, y_r, z_r)$  to describe the source and receiving spaces, we separate the origins of these two coordinate systems by a longitudinal distance  $L$  and we distribute the source and receiving points in such a way that there is no overlapping between these spaces. Several examples of source and receiving point distributions are shown in Figs 1(b-d). We arrange the source points as an array of  $p_x \times p_y$  points in a transverse plane and space them from each other by distances  $d_x$  and  $d_y$  along the  $x_s$  and  $y_s$  directions, resulting in a source plane with dimensions  $X_s = (p_x - 1)d_x$  and  $Y_s = (p_y - 1)d_y$ . In this plane, we compute the required source function  $|\Psi_T\rangle$  according to Eq. (3). The receiving points, on the other hand, are distributed in a 2D or 3D domain where we define their amplitude values according to a target light intensity profile  $|\Phi_T|^2$ . In Fig. 1(b), the receiving points are distributed in the horizontal plane  $y_r = 0$  as an array of  $p_{x,r} \times p_{z,r}$  points. They are spaced from each other by distances  $d_{x,r}$  and  $d_{z,r}$  along the  $x_r$  and  $z_r$  directions, leading to a horizontal plane with dimensions  $X_r = (p_{x,r} - 1)d_{x,r}$  and  $Z_r = (p_{z,r} - 1)d_{z,r}$ . A 3D distribution of receiving points is shown in Fig. 1(c) in which a set of  $p_{y,r}$  horizontal receiving planes are uniformly spaced from each other by a distance  $d_{y,r}$ . Non-Cartesian distributions are also possible in our wavefront shaping method as depicted in Fig. 1(d). In this case the receiving points are disposed within a set of  $p_{z,r}$  rings placed along the optical

axis, uniformly spaced from each other by a distance  $d_{z,r}$ , forming the lateral surface a cylinder with radius  $R_r$  and longitudinal length  $Z_r$ . Along each ring, we uniformly place  $p_{\phi,r}$  receiving points.

The values of all the parameters we adopted for each source and receiving point distributions of Fig. 1 are listed in Table 1. Our choice for these values stems from the fact that we need to guarantee that the resulting wave created by the  $N_S$  source points over the entire receiving space is essentially the same as if we had a continuous source. A maximum allowed value for the source spacing distances  $d_x$  and  $d_y$  can be derived to satisfy this requirement (see Supplementary Note 3). The coupling strengths  $|s_j|^2$  in order of decreasing size of their magnitude associated with the distribution of Fig. 1(a) are shown in Fig. 2(a) for different values of the separation distance  $L$  and in Fig. 2(b) for different values of the source plane  $y$ -dimension  $Y_s$ . In Fig. 2(c) we show the normalized intensity profile of the first six odd-numbered communication modes associated with the red dashed curve of Fig. 2(b) at the source plane (on the left of each sub-figure) and at the receiving horizontal plane (on the right). As expected for this distribution, the intensity profiles of the source eigenfunctions are symmetric with respect to the  $y_s = 0$  axis. Additionally, the receiving eigenfunctions do not correspond to any of the standard beams (e.g., Bessel, Airy beams). Finally, notice that the coupling strength curves are closely characterized by a series of steps. After these steps, the singular values decrease in a rapid fall-off fashion. The width of each step, which is increased by reducing the distance  $L$ , corresponds to the number of effective transverse modes along the receiving plane  $x_r$  direction. On the other hand, the number of steps, which is increased by either reducing the distance  $L$  or increasing the source plane  $Y_s$  dimension, corresponds to the number of effective longitudinal modes along the  $z_r$  direction. This is illustrated in Fig. 2(d) which shows the normalized intensity profile of the last mode of each of the first three steps of the red dashed curve of Fig. 2(b). A complete analysis of the intensity profiles of the communication modes and their coupling strengths for all the distribution examples of Fig. 1 is provided in Supplementary Note 4.

Next we apply Eqs. (3) and (4) to structure waves in the receiving space. We first consider the source and receiving space configuration of Fig. 1(b) parameterized accordingly to Table 1. The dimensions of these spaces are depicted in Fig. 3(a). We also consider the binary 2D image shown in Fig. 3(b) as our target receiving intensity profile  $|\Phi_T|^2$ . To project the entire target profile content onto the range of well-coupled modes of the receiving space set, we first need to modulate the target amplitude profile with a phase front of the form  $\exp(iQz_r)$ , in which  $Q$

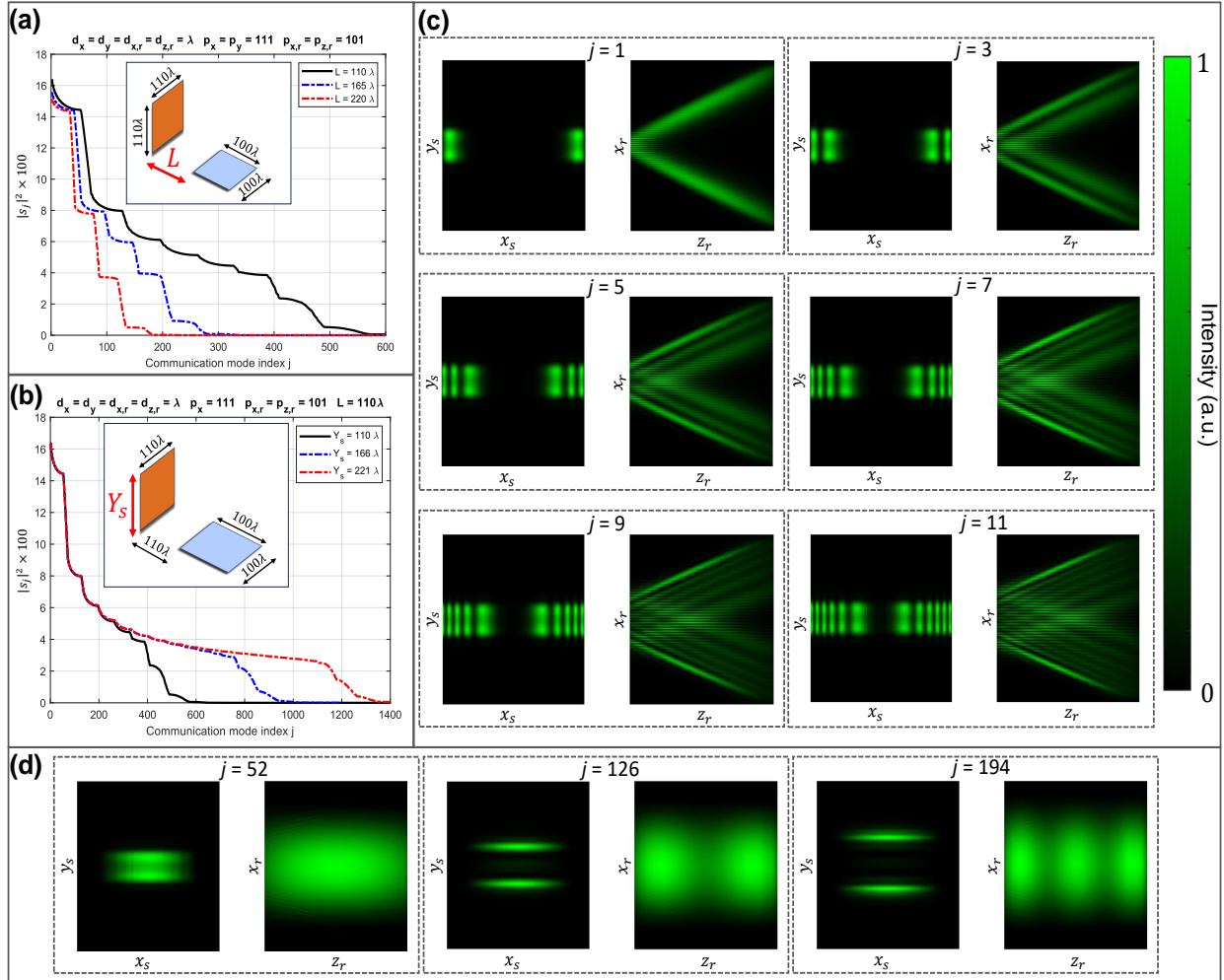


**Figure 2: Communication modes and their coupling strengths associated with a transverse source plane and a horizontal receiving plane.** Coupling strengths in order of decreasing size of their magnitude for (a) different values of the longitudinal separation distance  $L$  between the spaces and (b) for different values of the source plane  $y$ -dimension  $Y_s = (p_y - 1)d_y$ . The other parameters, remained fixed, are shown at the title of each sub-figure and follows Table 1. The coupling strength curves are closely characterized by a series of steps after which the singular values decrease in a rapid fall-off fashion. The width of each step and the number of steps corresponds respectively to the number of effective transverse and longitudinal modes. Normalized squared amplitude of (c) the first six odd-numbered communication modes and (d) the last mode of each of the first three steps of the red dashed line of (b). In each sub-figure in (c) and (d), the source eigenfunction is shown on the left and its associated receiving eigenfunction on the right.

is a positive real constant with  $Q \leq k$ . We do this because we understand that any wave we generate from our source plane is physically going to have predominantly some such underlying phase variation along the  $z$  direction, and so we can only reasonably generate patterns that have a similar underlying phase variation. Just what form we choose for this underlying phase variation is an empirical one so that we can best reasonably generate our patterns of interest using only strongly coupled communication modes. This is demonstrated in Fig. 3(c) in which the blue dots represent the amplitude of the inner product coefficients between the receiving eigenfunctions  $\{|\Phi_{R,j}\rangle\}$  and the modulated target profile  $\Phi_T \exp(iQz_r)$ , with  $Q = 0.95k$ . For reference, we also show the coupling strengths  $|s_j|^2$  (in arbitrary units) in the red dashed line. The required source squared amplitude  $|\Psi_T|^2$  and the resulting wave intensity  $|\phi|^2$ , computed using the first 1200 modes ( $j \leq 1200$ ), are shown in Fig. 3(d). Incorporation of the phase front  $\exp(iQz_r)$  results in a source function profile  $|\Psi_T|^2$  with an increased extent  $\Delta Y$  along the source plane  $y_s$  dimension, capable of rendering waves with high longitudinal spatial frequencies within the receiving space, giving rise to a resulting wave that fully resolves the target amplitude profile  $|\Phi_T|$ . This phase front is further discussed in Supplementary Note 5 in which we also relate the extent  $\Delta Y$  of the source profile with the characteristic minimum length of wave field (minimum spot)  $\Delta z$  that we can create along the longitudinal direction at a certain position  $z_0$  from our finite source transverse aperture.

**Experimental Generation** To optically reconstruct our structured light waves based on communication modes, we employed a phase-only reflective SLM (SANTEC 200) with pixel pitch  $\delta = 8 \mu\text{m}$  and 1,920 x 1,200 resolution. The operating wavelength is  $\lambda = 532 \text{ nm}$  (visible wavelength). First, as illustrated in Fig. 3(e), we compute the resulting wave at the plane  $z_s = L$ , i.e.,  $\phi(x_s, y_s, L)$  from Eq. (4). We then convert its complex field into a phase-only mask using a phase retrieval algorithm (Supplementary Note 6). Finally, before encoding the CGH to the SLM, we add a blazed grating profile to the phase-only mask to operate off-axis, separating the hologram's spectrum from the SLM zeroth diffraction order in  $k$  space. Our experimental setup is shown in Fig. 3(f). First, the laser beam is expanded and collimated to illuminate the entire SLM screen as a uniform plane-like wave. After the SLM, we place a standard  $4f$  lens system whose purpose is to recover the complex field  $\phi(x_s, y_s, L)$  at the front focal plane of the second lens. The first lens performs a Fourier transform operation, projecting the phase mask spectrum (which contains both amplitude and phase information) at the Fourier plane, i.e., at the mutual focal point plane of the two lenses. In this plane, we place an iris to spatially filter the desired spectrum, encoded on the first diffraction order of the incoming beam, while blocking the undesired zeroth diffraction order in  $k$ -space. The second lens performs an inverse Fourier operation, transforming the filtered

spectrum into real space, recovering the complex field  $\phi(x_s, y_s, L)$  in the front focal plane of this lens. Using a charge-coupled device ( $\mu$ Eye UI224SE-M, 1,280 x 1,024 resolution and 4.65  $\mu\text{m}$  pixel size), mounted on a translational stage (Thorlabs LTS150), we record transverse intensity distributions of the resulting wave at different  $z_r$  positions. Stacking these transverse distributions, we obtain the optical reconstruction of the resulting wave intensity. Because the SLM pixel pitch is much larger than the incident wavelength ( $\delta \approx 15\lambda$ ), the encoded phase mask occupies an area significantly larger than that of our source plane with dimensions  $X_s \times Y_s$ . As a result of this scaling up process, the aspect ratio between the transverse and longitudinal dimensions of our measured light wave does not follow the original 1:1 aspect ratio of the simulated resulting wave in the receiving space (see Supplementary Note 7 for details). Although an aspect ratio closer to 1:1 can be achieved by setting a  $4f$  lens configuration with a high de-magnification (Supplementary Note 7), we chose  $f_1 = 400$  mm and  $f_2 = 300$  mm to facilitate the measurements of the transverse intensity distributions and thus the optical reconstruction of the light waves.

**Results** For all the examples shown in this section, the projection of the target profile  $\Phi_T$  onto the set of receiving eigenfunctions is done by modulating  $\Phi_T$  with the phase front  $\exp(iQz_r)$  with  $Q = 0.95k$ . First, examples of different 2D structured light waves using the first 1200 communication modes associated with the source and receiving space configuration of Fig. 3(a) are compiled in Fig. 4. On the left of each sub-figure, we show the target receiving amplitude  $|\Phi_T|$ ; in the middle, the simulated resulting wave intensity  $|\phi|^2$  at the receiving horizontal plane; and on the right, the optical reconstructed wave using the optical setup of Fig. 3(f). Figs. 4(a-b) exhibit examples of target binary images containing bright digits on a dark background, while examples involving dark geometric shapes on a bright background and a checkerboard pattern are shown in Figs 4(c-d). These four examples demonstrate that our wavefront shaping method based on optimal orthogonal communication modes is able to provide high intensity uniformity in both dark and bright regions, resulting in reconstructed patterns with high contrast. Finally, in Fig. 4(e), we provide an example involving a target grayscale image containing features with high spatial frequencies. Notice that the fine rectangular features located in the middle of the receiving plane (which represent the rain drops) present a better reconstruction than the rectangular features located at the end of the receiving plane (that represent the sun rays). This phenomenon is intrinsically due to the finite dimension  $Y_s$  of our source aperture and is independent of the modes (or basis functions) used to create the structured light wave. In particular, the characteristic minimum length of wave field  $\Delta z$  that our (finite) source aperture can create varies along the longitudinal position  $z_r$  of the receiving space, being higher for points located further away from the source plane (see Supplementary

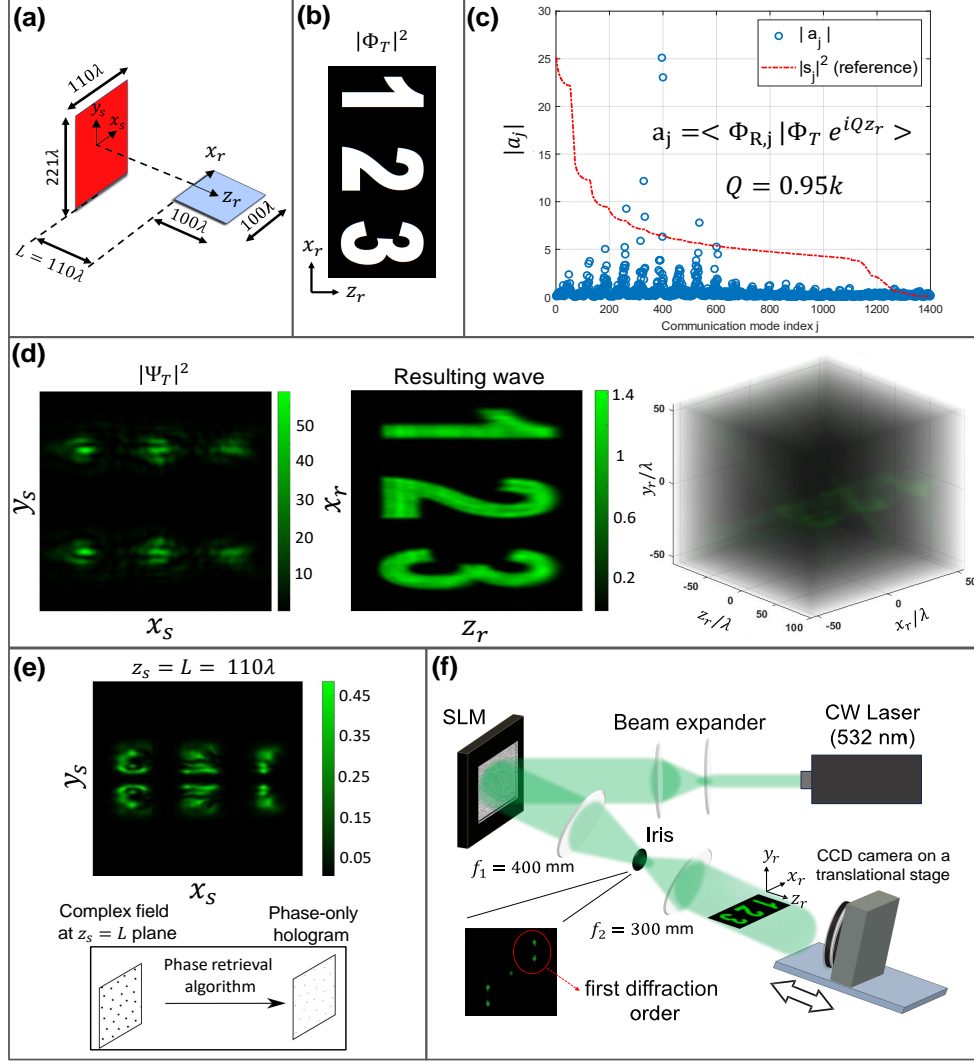


**Figure 3: Optical reconstruction of structured light waves based on communication modes using a reflective phase-only SLM.** For a given source and receiving space configuration (a), we compute the associated communication modes and their coupling strengths. (b) We define a target light intensity distribution (c) and project it onto the set of receiving eigenfunctions. (d) We compute the required source function  $\Psi_T$  at the source plane and its associated resulting wave  $\phi$  within the receiving space. (e) Encoding process: we evaluate the resulting wave from the required source profile at the plane  $z_s = L$ , and convert its complex field distribution into a phase-only CGH by means of a phase retrieval algorithm. (f) Optical setup: after the SLM, we employ a standard  $4f$  lens system to recover the complex field  $\phi(x_s, y_s, L)$  at front focal plane of the second lens. At the Fourier plane (mutual focal point plane of the two lenses), an iris is used to filter the desired spectrum (encoded on the first diffraction) and to block the unmodulated SLM zeroth diffraction order. A CCD camera on a translational stage records transverse intensity distributions of the resulting wave at different longitudinal positions.



Note 5). To fully resolve these fine features in our wavefront shaping method, we would need to consider a source plane with a higher dimension  $Y_s$  and with a denser array of source points for this additional increment in the dimension  $Y_s$  to satisfy the criteria for the source spacing distances (Supplementary Note 3).

Next we present examples of 3D structured light waves computed using the first 3500 modes associated with the source and receiving space configuration of Fig. 1(c) and parameterized as listed in Table 1. First, we project eight distinct digits, from '1' to '8', assigning each digit binary amplitude profile to one of the eight inner horizontal receiving planes. In Fig. 5(a) we show the target receiving intensity profile  $|\Phi_T|^2$  and the intensity of the corresponding required source function  $|\Psi_T|^2$ . The optical reconstruction of the resulting wave using a phase-only SLM is shown in Fig. 5(b), in which we can clearly identify and distinguish all eight digits, indicating the low level of crosstalk between their reconstructed intensity profiles, which can also be evidenced from transverse planes of the optical reconstruction as seen in the same figure at the mid ( $z_r = Z_r/2$ ) and quarter ( $z_r = Z_r/4$ ) longitudinal distances. In Fig. 5(c), we compare the measured and simulated results of the structured light wave intensity for all eight inner horizontal receiving planes. Notice that all the digits are reconstructed with high fidelity, presenting high intensity uniformity and contrast. An additional example of a structured light wave involving the projection of eight layers of an ellipsoid is provided and discussed in Supplementary Note 8. All these examples illustrate how powerful our wavefront shaping method is in creating structured light waves with continuous depth of field, high fidelity, and low cross-talk in a set of horizontal planes uniformly spaced by a measured distance less than 0.4 mm. To give a comparison, the light sheet wavefront shaping method can only provide reconstructed intensity profiles with reasonable low level of cross-talk when its light sheet beams are spaced from each other by a distance larger than 3 mm, as demonstrated in Fig. S9 of the Supplementary material of Ref. 44 in which the four digits "1 2 3 4" are projected onto four horizontal planes.

Creating structured light waves in a set of horizontal receiving planes with a tight spacing distance  $d_{y,r}$  between them is inevitably restricted by diffraction limits. Specifically, we are not able to maintain reconstructed intensity profiles with continuous depth of field, i.e., high axial resolution, for all the horizontal planes without introducing cross-talk. This scenario is explored in Supplementary Note 9 in which we reduce the separation distance from  $d_{y,r} = 15\lambda$  to  $d_{y,r} = 8\lambda$ . Finally, an example of a structured light wave projected onto the receiving cylindrical surface of Fig. 1(d) and parameterized as listed on Table 1 is presented and discussed in Supplementary Note

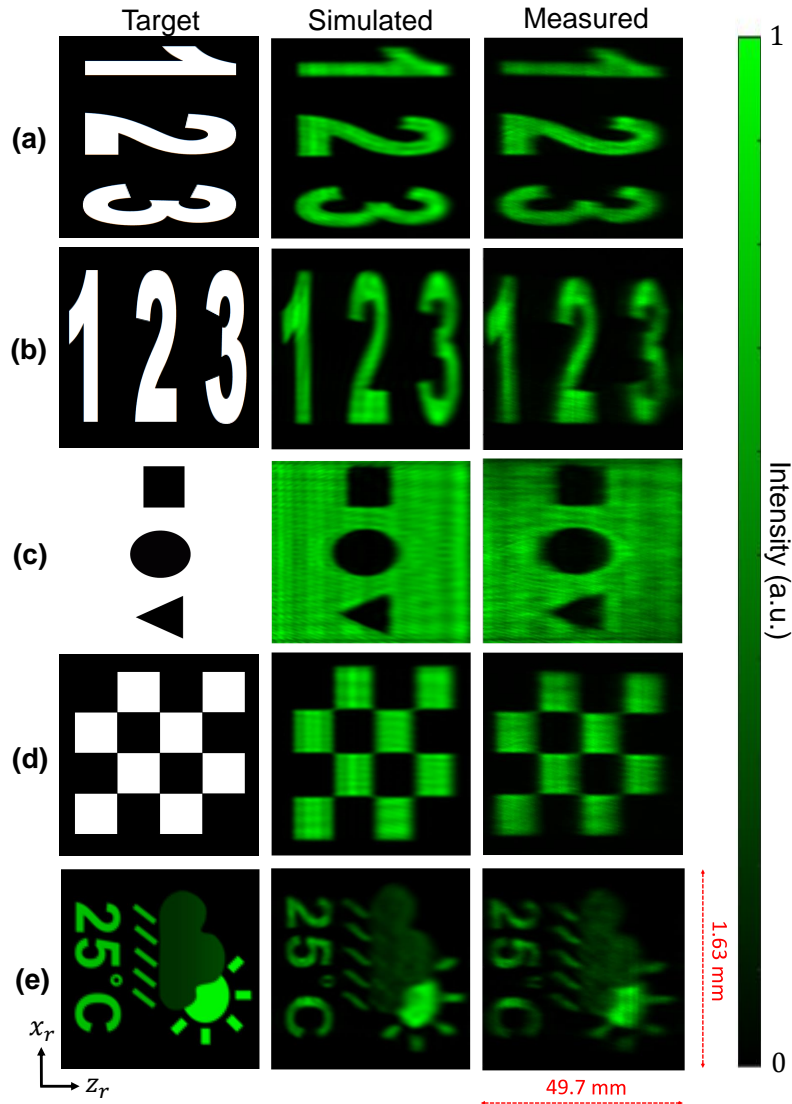


**Figure 4: Examples of 2D structured light waves projected in a horizontal receiving plane.** The structured light waves are computed from the first 1200 well coupled communication modes associated with the source and receiving space configuration of Fig. 1(b) with parameters listed on Table 1. From left to right: target receiving amplitude, simulated resulting wave intensity at the receiving horizontal plane, and optical reconstruction of the resulting wave using a phase-only SLM. **(a-b)** Bright digits on a dark background with distinct orientations. **(c)** Dark geometric shapes on a bright background. **(d)** A checkerboard pattern. **(e)** A grayscale image. Measured dimensions of the horizontal receiving plane are  $Z_r \times X_r = 49.7 \text{ mm} \times 1.63 \text{ mm}$ .

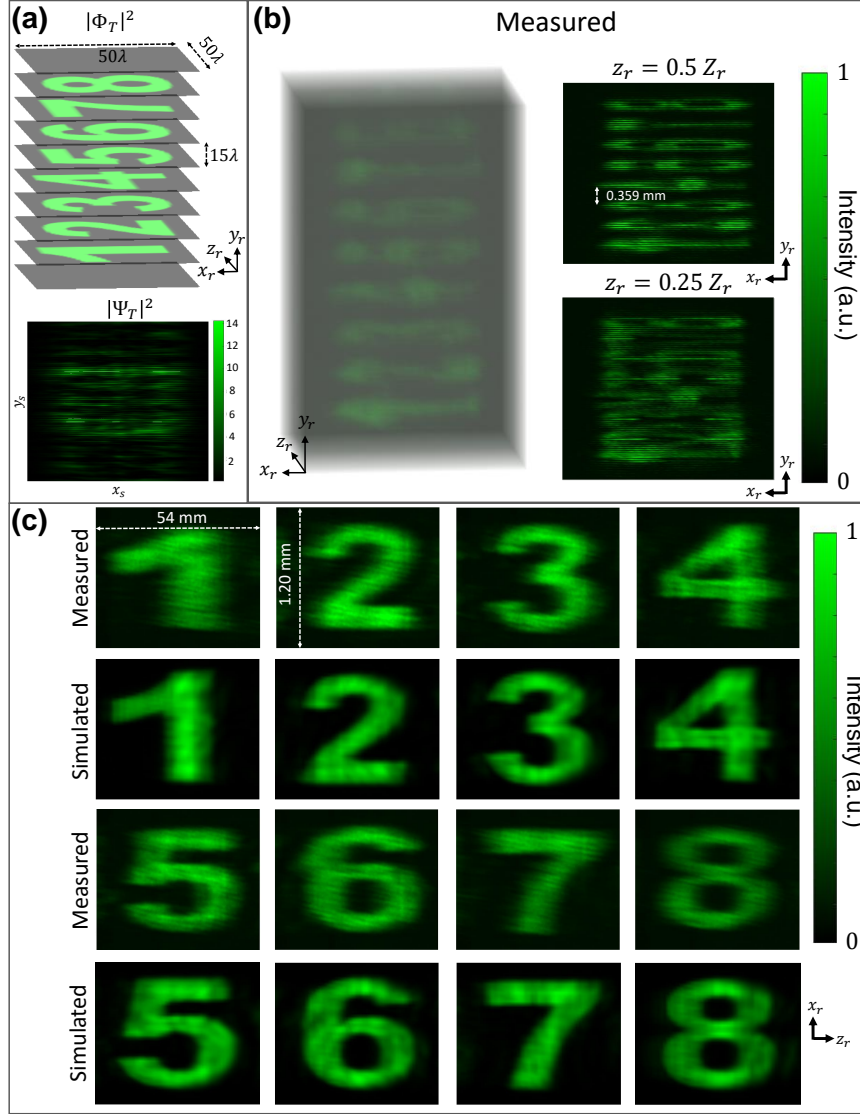


**Figure 5: Example of a 3D structured light wave projected in a set of uniformly spaced horizontal receiving planes.** Projecting eight digits within the eight inner horizontal receiving planes of the source-receiving space system of Fig. 1(c) with parameters listed on Table 1. The required source function and the resulting wave are computed using the first 3500 modes. **(a)** Target receiving profile  $|\Phi_T|^2$  intensity and corresponding required source function  $|\Psi_T|^2$  intensity. **(b)** Optical reconstruction of the resulting wave using a phase-only SLM within a volume containing the horizontal receiving planes and at transverse planes located at the mid and quarter longitudinal distances,  $z_r = Z_r/2$  and  $z_r = Z_r/4$  ( $Z_r$ : longitudinal length of the planes). The measured spacing distance between the horizontal planes is  $d_{y,r} = 0.359 \text{ mm}$ . **(c)** Comparison between measured and simulated results of all the eight reconstructed digits. Measured dimensions of the horizontal planes are  $Z_r \times X_r = 54 \text{ mm} \times 1.20 \text{ mm}$ .

10. Our result shows that our optimum orthogonal communication modes lead to a resulting wave with no undesired intensity along the optical axis, a feature that is difficult to achieve with the light sheet wavefront method in which the Bessel modes arranged along a ring unavoidably create a high intensity spot at the center of the ring.

### 3 Discussion

We introduced and experimentally verified a new wavefront shaping method based on interfering the optimum orthogonal communication modes connecting a source plane and a receiving volume. Each communication mode encompasses a pair of eigenfunctions, one in the source space and another one in the receiving space, both computed by means of the singular value decomposition modal optics. The orthogonality and optimization properties of the source and receiving eigenfunctions over the entire source and receiving spaces provide 2D and 3D structured light waves with high fidelity, high contrast and with minimal level of cross-talk, allowing these structured light waves to be perceived from different angles and thus being potentially employed in volumetric displays and AR/VR headsets. Additionally, our method could be favorable in applications that require controlling light's intensity within a 3D domain with high precision, notably in materials processing and in optical trapping. For instance, our method can potentially be employed to manipulate many micro-particles simultaneously in a set of horizontal planes with precise control. Our method can also be suitable for real-time holography or applications that require dynamic wavefront shaping. This is aided by the low computational cost associate with our method. The coupled modes connecting the source and receiver spaces are computed once, then any target object can be synthesized through a Fourier-like matrix operation which can be parallelized using GPUs.

Although we limited our analysis to a fixed operating wavelength, our method can be extended to create spatiotemporal structured light waves by considering a full time-dependent Green's function for the coupling operator. Furthermore, light waves with spatially varying polarization states can also be created by adopting a dyadic vector potential Green's function instead of a scalar one<sup>48</sup>. In all these cases, metasurfaces<sup>55,56</sup> are an ideal wavefront shaping platform as they offer both multi-wavelength control and polarization transformations at the nanoscale<sup>56</sup>. The sub-wavelength regime of the flat-optics platform also benefits our wavefront shaping method in creating reconstructed light waves with the same aspect ratio designed for the target 3D light distribution without the need of setting a high de-magnification for the  $4f$  system. Therefore, in a future work, our wavefront shaping method can be implemented with metasurface platforms to achieve

control over other degrees-of-freedom of light, unlocking new applications in digital holography and structured light, as well as light-matter interaction, classical and quantum communications, and beyond. Finally, because our method is based on the interfering of communication modes that leads to the optimal construction of any target field distribution, it can also be used as a benchmark to analyze the limitations of existing wavefront shaping techniques. If our method fails to create a desired field distribution, it indicates that this distribution cannot be achieved with any other technique.

**Acknowledgements** V.S.A acknowledges financial support from the Coordination of Superior Level Staff Improvement (CAPES), grant no. 88887.833874/2023-00, and from the National Council for Scientific and Technological Development (CNPq), grant no. 140270/2022-1. A.H.D acknowledges the support of the Optica Foundation. L.A.A. acknowledges financial support from the National Council for Scientific and Technological Development (CNPq), grant no. 309201/2021-7, and from the São Paulo Research Foundation (FAPESP), grant no. 2020/05280-5. F.C. acknowledges financial support from the Office of Naval Research (ONR) under the MURI programme, grant no. N00014-20-1-2450, and from the Air Force Office of Scientific Research (AFOSR) under grant nos FA9550-21-1-0312 and FA9550-22-1-0243. D. M. also acknowledges support from AFOSR grant FA9550-21-1-0312.

**Competing Interests** The authors declare no competing interests.

## 4 References

1. Wang, J. & Liang, Y. Generation and Detection of Structured Light: A Review. *Frontiers in Physics* **9**, 263 (2021).
2. He, C., Shen, Y. & Forbes, A. Towards higher-dimensional structured light. *Light: Science & Applications* **11**, 205 (2022).
3. Laucht, A. *et al.* Roadmap on quantum nanotechnologies. *Nanotechnology* **32**, 162003 (2021).
4. Wan, Z., Wang, H., Liu, Q., Fu, X. & Shen, Y. Ultra-degree-of-freedom structured light for ultracapacity information carriers. *ACS Photonics* **10**, 2149–2164 (2023).
5. Grier, D. G. A revolution in optical manipulation. *Nature* **424**, 810–816 (2003).

6. Kumar, S. & Singh, R. Recent optical sensing technologies for the detection of various biomolecules: Review. *Optics & Laser Technology* **134**, 106620 (2021).
7. Lee, M., Hugonnet, H., Lee, M. J., Cho, Y. & Park, Y. Optical trapping with holographically structured light for single-cell studies. *Biophysics Reviews* **4**, 011302 (2023).
8. Genevet, P. & Capasso, F. Holographic optical metasurfaces: a review of current progress. *Reports on Progress in Physics* **78**, 024401 (2015).
9. Quevedo-Teruel, O. *et al.* Roadmap on metasurfaces. *Journal of Optics* **21**, 073002 (2019).
10. Huang, L., Zhang, S. & Zentgraf, T. Metasurface holography: from fundamentals to applications. *Nanophotonics* **7**, 1169–1190 (2018).
11. Wan, Z., Shi, Z., Liu, Q. & Fu, X. Holographic tailoring of structured light field with digital device. *Photonics* **9** (2022).
12. Sedeh, H. B. & Litchinitser, N. M. Singular optics empowered by engineered optical materials. *Nanophotonics* **12**, 2687–2716 (2023).
13. Kuznetsov, A. I. *et al.* Roadmap for optical metasurfaces. *ACS Photonics* **11**, 816–865 (2024).
14. Allen, L., Beijersbergen, M. W., Spreeuw, R. J. C. *et al.* Orbital angular momentum of light and the transformation of laguerre-gaussian laser modes. *Phys. Rev. A* **45**, 8185–8189 (1992).
15. Siegman, A. E. Hermite–gaussian functions of complex argument as optical-beam eigenfunctions. *J. Opt. Soc. Am.* **63**, 1093–1094 (1973).
16. Bandres, M. A. & Gutiérrez-Vega, J. C. Ince–gaussian beams. *Opt. Lett.* **29**, 144–146 (2004).
17. Pinnell, J., Nape, I., Sephton, B. *et al.* Modal analysis of structured light with spatial light modulators: a practical tutorial. *J. Opt. Soc. Am. A* **37**, C146–C160 (2020).
18. Gerchberg, R. W. A practical algorithm for the determination of phase from image and diffraction plane pictures. *Optik* **35**, 237–246 (1972).
19. Forbes, A., de Oliveira, M. & Dennis, M. R. Structured light. *Nature Photonics* **15**, 253–262 (2021).
20. Piccardo, M., Ginis, V., Forbes, A. *et al.* Roadmap on multimode light shaping. *Journal of Optics* **24**, 013001 (2021).

21. Park, J.-H. Recent progress in computer-generated holography for three-dimensional scenes. *Journal of Information Display* **18**, 1–12 (2017).
22. Pi, D., Liu, J. & Wang, Y. Review of computer-generated hologram algorithms for color dynamic holographic three-dimensional display. *Light: Science & Applications* **11**, 231 (2022).
23. Tsang, P. W. M., Poon, T.-C. & Wu, Y. M. Review of fast methods for point-based computer-generated holography [invited]. *Photon. Res.* **6**, 837–846 (2018).
24. Zhang, Y., Fan, H., Wang, F., Gu, X., Qian, X. & Poon, T.-C. Polygon-based computer-generated holography: a review of fundamentals and recent progress [invited]. *Appl. Opt.* **61**, B363–B374 (2022).
25. Bayraktar, M. & Özcan, M. Method to calculate the far field of three-dimensional objects for computer-generated holography. *Appl. Opt.* **49**, 4647–4654 (2010).
26. Okada, N., Shimobaba, T., Ichihashi, Y. *et al.* Band-limited double-step fresnel diffraction and its application to computer-generated holograms. *Opt. Express* **21**, 9192–9197 (2013).
27. Zhao, Y., Cao, L., Zhang, H. *et al.* Accurate calculation of computer-generated holograms using angular-spectrum layer-oriented method. *Opt. Express* **23**, 25440–25449 (2015).
28. Chen, J.-S. & Chu, D. P. Improved layer-based method for rapid hologram generation and real-time interactive holographic display applications. *Opt. Express* **23**, 18143–18155 (2015).
29. Zhang, H., Cao, L. & Jin, G. Computer-generated hologram with occlusion effect using layer-based processing. *Appl. Opt.* **56**, F138–F143 (2017).
30. Makey, G., Yavuz, Ö., Kesim, D. K., Turnalı, A., Elahi, P., Ilday, S., Tokel, O. & Ilday, F. Ö. Breaking crosstalk limits to dynamic holography using orthogonality of high-dimensional random vectors. *Nature Photonics* **13**, 251–256 (2019).
31. Pang, Y., Cao, A., Wang, J. *et al.* Simple encoding method of phase-only hologram for low crosstalk full-color multi-plane holographic projection. *Optics and Lasers in Engineering* **147**, 106748 (2021).
32. Velez-Zea, A., Barrera-Ramírez, J. F. & Torroba, R. Improved phase hologram generation of multiple 3d objects. *Appl. Opt.* **61**, 3230–3239 (2022).

33. Wang, Z., Chen, T., Chen, Q., Tu, K., Feng, Q., Lv, G., Wang, A. & Ming, H. Reducing crosstalk of a multi-plane holographic display by the time-multiplexing stochastic gradient descent. *Opt. Express* **31**, 7413–7424 (2023).
34. Wang, J., Wang, J., Zhou, J., Zhang, Y. & Wu, Y. Crosstalk-free for multi-plane holographic display using double-constraint stochastic gradient descent. *Opt. Express* **31**, 31142–31157 (2023).
35. Zamboni-Rached, M. Stationary optical wave fields with arbitrary longitudinal shape by superposing equal frequency Bessel beams: Frozen waves. *Optics Express* **12**, 4001–4006 (2004).
36. Vieira, T. A., Gesualdi, M. R. R. & Zamboni-Rached, M. Frozen waves: experimental generation. *Opt. Lett.* **37**, 2034–2036 (2012).
37. Čižmár, T. & Dholakia, K. Tunable bessel light modes: engineering the axial propagation. *Opt. Express* **17**, 15558–15570 (2009).
38. Dorrah, A. H., Zamboni-Rached, M. & Mojahedi, M. Controlling the topological charge of twisted light beams with propagation. *Phys. Rev. A* **93**, 063864 (2016).
39. Dorrah, A. H., Rubin, N. A., Tamagnone, M., Zaidi, A. & Capasso, F. Structuring total angular momentum of light along the propagation direction with polarization-controlled meta-optics. *Nature Communications* **12**, 6249 (2021).
40. Dorrah, A. H., Palmieri, A., Li, L. & Capasso, F. Rotatum of Light. *arXiv e-prints* arXiv:2310.16317 (2023). 2310.16317.
41. Dorrah, A. H., Rubin, N. A., Zaidi, A., Tamagnone, M. & Capasso, F. Metasurface optics for on-demand polarization transformations along the optical path. *Nature Photonics* **15**, 287–296 (2021).
42. Ambrosio, L. A. Millimeter-structured nondiffracting surface beams. *J. Opt. Soc. Am. B* **36**, 638–645 (2019).
43. de Sarro, J. O. & Ambrosio, L. A. Surface beams resistant to diffraction and attenuation and structured at the millimeter scale. *J. Opt. Soc. Am. B* **38**, 677–684 (2021).
44. Dorrah, A. H., Bordoloi, P., de Angelis, V. S. *et al.* Light sheets for continuous-depth holography and three-dimensional volumetric displays. *Nature Photonics* **17**, 427–434 (2023).



45. Asoudegi, N., Dorrah, A. H. & Mojahedi, M. Deep learning-assisted light sheet holography. *Opt. Express* **32**, 1161–1175 (2024).
46. Miller, D. A. B. Spatial channels for communicating with waves between volumes. *Opt. Lett.* **23**, 1645–1647 (1998).
47. Piestun, R. & Miller, D. A. B. Electromagnetic degrees of freedom of an optical system. *J. Opt. Soc. Am. A* **17**, 892–902 (2000).
48. Miller, D. A. B. Waves, modes, communications, and optics: a tutorial. *Adv. Opt. Photon.* **11**, 679–825 (2019).
49. SeyedinNavadeh, S., Milanizadeh, M., Zanetto, F. *et al.* Determining the optimal communication channels of arbitrary optical systems using integrated photonic processors. *Nature Photonics* **18**, 149–155 (2024).
50. Miller, D. A. B. Establishing optimal wave communication channels automatically. *Journal of Lightwave Technology* **31**, 3987–3994 (2013).
51. Miller, D. A. B. Communicating with waves between volumes: evaluating orthogonal spatial channels and limits on coupling strengths. *Appl. Opt.* **39**, 1681–1699 (2000).
52. Martinsson, P., Ma, P., Burvall, A. & Friberg, A. T. Communication modes in scalar diffraction. *Optik* **119**, 103–111 (2008).
53. Martinsson, P., Lajunen, H., Ma, P. & Friberg, A. T. Communication modes in vector diffraction. *Optik* **121**, 2087–2093 (2010).
54. Burvall, A., Martinsson, P. & Friberg, A. T. Communication modes applied to axicons. *Opt. Express* **12**, 377–383 (2004).
55. Yu, N. & Capasso, F. Flat optics with designer metasurfaces. *Nature Materials* **13**, 139–150 (2014).
56. Dorrah, A. H. & Capasso, F. Tunable structured light with flat optics. *Science* **376**, eabi6860 (2022).

Table 1: Number of source and receiving points, their spacing distances and the longitudinal separation between the source and receiving spaces for each example of source and receiving space configuration of Fig. 1. For the example of Fig. 1(d), we present the radius  $R_r$  of each ring that compose the receiving surface. The separation distance of the receiving points along each ring is  $d_{\phi,r} = (2\pi/p_{\phi,r})R_r = 1.55\lambda$ , which corresponds to an angular separation of  $3.56^\circ$ .

Configuration	Source Plane		$L$	Receiving space	
	$p_x \times p_y$	$d_x, d_y$		array of points	spacing distances
Fig.1(b)	$111 \times 222$	$\lambda$	$110\lambda$	$p_{x,r} \times p_{z,r} = 101 \times 101$	$d_{x,r} = d_{y,r} = d_{z,r} = \lambda$
Fig.1(c)	$111 \times 301$	$0.5\lambda$	$50\lambda$	$p_{x,r} \times p_{z,r} = 51 \times 51$ $p_{y,r} = 10$	$d_{x,r} = d_{z,r} = \lambda$ $d_{y,r} = 15\lambda$
Fig.1(d)	$201 \times 201$	$0.5\lambda$	$50\lambda$	$p_{z,r} = 101$ $p_{\phi,r} = 101$	$d_{z,r} = 0.5\lambda$ $R_r = 25\lambda$

# Supplementary Information

## Optimal structured light waves generation in 3D volumes using communication mode optics

Vinicius S. de Angelis<sup>1,2</sup>, Ahmed H. Dorrah<sup>1</sup>, Leonardo A. Ambrosio<sup>2</sup>, David A. B. Miller<sup>3</sup>, and Federico Capasso<sup>1,\*</sup>

<sup>1</sup>*Harvard John A. Paulson School of Engineering and Applied Sciences, Harvard University, Cambridge, MA 02138, USA*

<sup>2</sup>*Department of Electrical and Computer Engineering, São Carlos School of Engineering, University of São Paulo, 400 Trabalhador são-carlense Ave., 13566-590, São Carlos, São Paulo, Brazil*

<sup>3</sup>*Ginzton Laboratory, Stanford University, Stanford, CA 94305, USA*

*\*Corresponding author: capasso@seas.harvard.edu*

### Contents

<b>Supplementary Note 1: Singular value decomposition and maximization property of the communication modes</b>	<b>3</b>
<b>Supplementary Note 2: Required source function for a given target light distribution</b>	<b>7</b>
<b>Supplementary Note 3: Maximum allowed value for the distances between the source points</b>	<b>8</b>
<b>Supplementary Note 4: Coupling strengths and intensity profiles of communication modes</b>	<b>11</b>
<b>Supplementary Note 5: Characteristic minimum longitudinal length of wave field generated by a finite source transverse plane</b>	<b>21</b>

<b>Supplementary Note 6: Phase retrieval algorithm</b>	<b>26</b>
<b>Supplementary Note 7: Aspect ratio of our reconstructed structured light waves</b>	<b>28</b>
<b>Supplementary Note 8: Projecting an ellipsoid</b>	<b>29</b>
<b>Supplementary Note 9: Reducing the separation distance between the horizontal receiving planes</b>	<b>31</b>
<b>Supplementary Note 10: Projecting structured light waves onto the longitudinal surface of a cylinder</b>	<b>33</b>
<b>Supplementary References</b>	<b>35</b>

## Supplementary Note 1: Singular value decomposition and maximization property of the communication modes

The source  $\{|\Psi_{S,j}\rangle\}$  and receiving  $\{|\Phi_{R,j}\rangle\}$  eigenfunctions are computed from the eigen-equations associated with the operators  $G_{SR}^\dagger G_{SR}$  and  $G_{SR} G_{SR}^\dagger$ :

$$G_{SR}^\dagger G_{SR} |\Psi_{S,j}\rangle = |s_j|^2 |\Psi_{S,j}\rangle, \quad (\text{S1a})$$

$$G_{SR} G_{SR}^\dagger |\Phi_{R,j}\rangle = |s_j|^2 |\Phi_{R,j}\rangle, \quad (\text{S1b})$$

in which the eigenvalues  $|s_j|^2$ , the squared amplitude of the singular values  $s_j$  of  $G_{SR}$ , are the same for both operators. Additionally, the eigenfunctions satisfy the following one-to-one relation between their eigen-spaces <sup>1</sup>:

$$G_{SR} |\Psi_{S,j}\rangle = s_j |\Phi_{R,j}\rangle. \quad (\text{S2})$$

The relations established in Eq. (S1) are the core of the singular value decomposition (SVD) modal optics and its communication modes <sup>1</sup>. Each source eigenfunction  $|\Psi_{S,j}\rangle$  in the source space creates a resulting wave in the receiving space that has the form of the receiving eigenfunction  $|\Phi_{R,j}\rangle$  weighted by the complex amplitude  $s_j$ .

Assuming that the source and the receiving spaces contain a finite number of source and receiving points,  $N_S$  and  $N_R$ , rearranging Eq. (S2) by isolating the coupling operator  $G_{SR}$ , we obtain the expression for the SVD of  $G_{SR}$ :

$$G_{SR} = \sum_{j=1}^{N_m} s_j |\Phi_{R,j}\rangle \langle \Psi_{S,j}|, \quad (\text{S3})$$

in which  $N_m$  is the smaller of  $N_S$  and  $N_R$ . From  $N_m < j \leq N_{\text{large}}$ , in which  $N_{\text{large}}$  is the larger of  $N_S$  and  $N_R$ , the singular values  $s_j$  are identically zero <sup>1</sup>. In matrix form, Eq. (S3) can be written as:

$$G_{SR} = V D_{\text{diag}} U^\dagger, \quad (\text{S4})$$

where  $V$  is a  $N_R \times N_m$  matrix whose columns are the receiving eigenfunctions  $|\Phi_{R,j}\rangle$ , with  $1 \leq j \leq N_m$ ;  $D_{\text{diag}}$  is a diagonal  $N_m \times N_m$  matrix whose diagonal elements are the singular values  $s_j$ ; and  $U$  is a  $N_S \times N_m$  matrix whose columns are the source eigenfunctions  $|\Psi_{S,j}\rangle$ . Additionally, an important property that comes from Eq. (S4) is that the sum  $S$  of the coupling strengths  $|s_j|^2$

is finite and it can be obtained directly from the elements  $g_{ij}$  [Eq. (2) in the main text] of  $G_{SR}$ , without solving its SVD, as:

$$S = \sum_{q=1}^{N_m} |s_j|^2 = \sum_{i=1}^{N_R} \sum_{j=1}^{N_S} |g_{ij}|^2. \quad (\text{S5})$$

Eq. (S5) tells us that the number of communication modes and their coupling strengths are bounded for a given distribution of source and receiving points. Additionally, the source and receiving eigenfunctions computed from Eq. (S4) are also unique to a particular distribution of source and receiver points. Therefore it is not possible to obtain more orthogonal communication modes by performing linear combinations of these eigenfunctions. To increase the number of communication modes, we must modify the distribution of source and receiving points, leading to a new coupling operator matrix and thus to another SVD solution <sup>1</sup>.

Now we derive the maximization properties of the communication mode pairs,  $\{|\Psi_{S,j}\rangle\}$  and  $\{|\Phi_{R,j}\rangle\}$ , computed from the eigen-equations of Eq. (S1). Our derivation follows the argument developed in Ref. 2 and it is based on finding which normalized source function  $\Psi_n(\mathbf{r}_S)$  (here the index  $n$  means normalized) gives rise to a resulting wave  $\phi(\mathbf{r}_R)$  in the receiving space with the largest possible magnitude  $|g|^2$ , here defined as:

$$|g|^2 = \int_{V_R} \phi^*(\mathbf{r}_R)\phi(\mathbf{r}_R)d^3\mathbf{r}_R, \quad (\text{S6})$$

in which  $V_R$  stands for a finite volume containing the receiving space.

We start by recalling that the resulting wave  $\phi(\mathbf{r}_R)$  associated with a source function  $\Psi_n(\mathbf{r}_S)$  is given by:

$$\phi(\mathbf{r}) = \int_{V_S} G_{RS}(\mathbf{r}, \mathbf{r}_S)\Psi_n(\mathbf{r}_S)d^3\mathbf{r}_S, \quad (\text{S7})$$

for a finite volume  $V_S$  containing the source space. Notice that Eq. (S7) is the integral form of Eq. (4) in the main text. Instead of a collection of source points, here we are assuming a continuous source function. Provided that our source points are close enough to each other, satisfying the criteria discussed in Supplementary Note 3, our derivation, based on continuous source and receiving functions, also applies for a collection of source and receiving points, analyzed in the main text. In view of that, substituting Eq. (S7) into Eq. (S6) yields:

$$|g|^2 = \int_{V_S} \Psi_n^*(\mathbf{r}'_S) \int_{V_S} K(\mathbf{r}'_S, \mathbf{r}_S)\Psi_n(\mathbf{r}_S)d^3\mathbf{r}'_S d^3\mathbf{r}_S, \quad (\text{S8})$$

in which we defined the kernel  $K(\mathbf{r}'_S, \mathbf{r}_S)$  as:

$$K(\mathbf{r}'_S, \mathbf{r}_S) = \int_{V_R} G_{RS}^*(\mathbf{r}_R, \mathbf{r}'_S) G_{RS}(\mathbf{r}_R, \mathbf{r}_S) d^3\mathbf{r}_R, \quad (\text{S9})$$

which constitutes an Hermitian operator since  $K(\mathbf{r}'_S, \mathbf{r}_S) = K^*(\mathbf{r}_S, \mathbf{r}'_S)$ . Additionally, this kernel satisfies the following property:

$$\int_{V_S} \int_{V_S} |K(\mathbf{r}'_S, \mathbf{r}_S)|^2 d^3\mathbf{r}'_S d^3\mathbf{r}_S < \infty, \quad (\text{S10})$$

as both the source and receiving spaces are assumed to be defined over finite volumes,  $V_S$  and  $V_R$ , and the kernel  $K(\mathbf{r}'_S, \mathbf{r}_S)$  is a continuous bounded function. Notice that we are assuming that the source and receiving spaces are completely separated from each other, with no overlapping between them, as illustrated from the distribution examples in Figs 1(b-d) in the main text. Consequently,  $K(\mathbf{r}'_S, \mathbf{r}_S)$  does not present any singularities as the term  $|\mathbf{r}_R - \mathbf{r}_S|$  in the expression of  $G_{RS}$  [see Eq. (1) in the main text] always yields non-zero values. Therefore, with Eq. (S10) holding true, it allows us to conclude that the kernel  $K(\mathbf{r}'_S, \mathbf{r}_S)$  constitutes a Hilbert-Schmidt operator<sup>1</sup>. Since all Hilbert-Schmidt operators are compact,  $K(\mathbf{r}'_S, \mathbf{r}_S)$  is a compact Hermitian operator and thus its eigenfunctions form a complete set in the source space and their eigenvalues are real numbers. These results are formally proved by functional analysis. See Ref. 1 for deeper discussion, and also Ref. 3 for an introduction to the necessary results from functional analysis. The compactness also allows us to conclude that, with a sufficiently dense set of points in the source and receiving spaces, the resulting point-wise source and receiver eigenfunctions from the matrix problem converge to the solutions of the continuous problem.

Multiplying both sides of Eq. (S8) by  $\Psi_n(\mathbf{r}'_S)$  results in:

$$|g|^2 \Psi_n(\mathbf{r}'_S) = \int_{V_S} K(\mathbf{r}'_S, \mathbf{r}_S) \Psi_n(\mathbf{r}_S) d^3\mathbf{r}_S, \quad (\text{S11})$$

where we have made use of our assumption that we are dealing with a normalized source function, i.e.,  $\int_{V_S} |\Psi_n(\mathbf{r}_S)|^2 d^3\mathbf{r}_S = 1$ . It can be shown that the solutions of the integral equation in Eq. (S11) for the largest possible values of  $|g|^2$  are given when we choose  $\Psi_n(\mathbf{r}_S)$  as the normalized eigenfunctions of the kernel  $K(\mathbf{r}'_S, \mathbf{r}_S)$ <sup>4</sup>. In fact, these eigenfunctions correspond to the normalized versions of our source eigenfunctions  $\{|\Psi_{n,S,j}\rangle\}$  and the largest successive values of  $|g|^2$  correspond to our eigenvalues  $|s_j|^2$ .

Therefore, by ordering our source eigenfunctions  $\{|\Psi_{S,j}\rangle\}$  by decreasing size of their corresponding eigenvalues  $|s_j|^2$  we notice that: the source function  $|\Psi_{S,1}\rangle$  leads to the largest possible

magnitude of wave vector in the receiving space and this wave vector has the form of the receiving function  $|\Phi_{R,1}\rangle$ . Similarly,  $|\Psi_{S,2}\rangle$  leads to the second largest possible magnitude of wave vector in the receiving space having the form of  $|\Phi_{R,2}\rangle$ . And we can proceed in a similar fashion for all the other source eigenfunctions. Thus, we can conclude that our communication mode pairs,  $\{|\Psi_{S,j}\rangle\}$  and  $\{|\Phi_{R,j}\rangle\}$ , are indeed the optimal modes that connect the source and receiving spaces in terms of magnitude of inner product. See Ref. 1 for an extended discussion of the properties of these operators and sets of eigenfunctions, and the SVD generally.



## Supplementary Note 2: Required source function for a given target light distribution

Let  $|\Phi_T\rangle$  be the our target profile in the receiving space  $H_R$ . In this space,  $|\Phi_T\rangle$  can be written as a linear superposition of the receiving eigenfunctions  $|\Phi_{R,j}\rangle$  as follows:

$$|\Phi_T\rangle = \sum_j a_j |\Phi_{R,j}\rangle, \quad (\text{S12})$$

in which the coefficients  $a_j$  are computed from the inner product between the target profile and the receiving eigenfunctions  $a_j = \langle \Phi_{R,j} | \Phi_T \rangle$ . Using the relation of Eq. (S2), we can determine the component of the source function that creates each component  $a_j |\Phi_{R,j}\rangle$  of the target profile:

$$G_{RS}(a_j |\Psi_{S,j}\rangle) = s_j (a_j |\Phi_{R,j}\rangle) \rightarrow G_{RS}\left(\frac{a_j}{s_j} |\Psi_{S,j}\rangle\right) = a_j |\Phi_{R,j}\rangle. \quad (\text{S13})$$

Therefore, summing up all these weighted source eigenfunctions  $(a_j/s_j) |\Psi_{S,j}\rangle$ , we obtain the required source function  $|\Psi_T\rangle$  in the source space  $H_S$  that creates the target profile  $|\Phi_T\rangle$  in the receiving space <sup>1</sup>:

$$|\Psi_T\rangle = \sum_j \frac{a_j}{s_j} |\Psi_{S,j}\rangle = \sum_j \frac{1}{s_j} \langle \Phi_{R,j} | \Phi_T \rangle |\Psi_{S,j}\rangle, \quad (\text{S14})$$

which corresponds to Eq. (3) in the main text.

### Supplementary Note 3: Maximum allowed value for the distances between the source points

The source points must be close enough to each other such that the collection of these points behaves similarly to a continuous source, i.e., a set of uniform source patches covering the entire source plane. In particular, we need to make sure that the resulting wave amplitude created by a point source  $(x_s, y_s)$  at a given receiving point  $(x_r, y_r, z_r)$  is approximately the same as the one created by a uniform source that surrounds that point source. To satisfy this condition, we consider two paths connecting a given receiving point, one from a corner of the patch and another one from the middle of the patch (where the source point is located), as illustrated in Fig. S1(a). The waves that leave these two points at the source aperture result in destructive interference at the receiving point if the difference between the two path lengths is half the wavelength. Therefore, it is reasonable to assume that if the difference between these paths is less than half a wavelength, there is no significant difference whether we consider a point source or a uniform source patch. From this condition, we derive an upper limit for the allowed values of the spacing distances between the source points  $d_x$  and  $d_y$ .

Assuming that the spacing between the source points along the  $x_s$  and  $y_s$  directions are the same, i.e.,  $d_x = d_y$ , from Fig. S1(a), the difference between the two path lengths is:

$$|L_{\text{corner}} - L_{\text{middle}}| = \sqrt{2}(d_y/2) \sin \theta, \quad (\text{S15})$$

in which  $\theta$  is the angle subtended between the path with length  $L_{\text{middle}}$  and the horizontal plane where the receiving point is located, such that:

$$\sin \theta = \frac{y_s - y_r}{\sqrt{(x_s - x_r)^2 + (y_s - y_r)^2 + (L + z_r)^2}}. \quad (\text{S16})$$

The maximum difference  $|L_{\text{corner}} - L_{\text{middle}}|$  in Eq. (S15) between the two paths, that occurs for a maximum value for  $\theta$ ,  $\theta_{\text{max}}$ , is associated with a path connecting a source point at a corner of the source aperture to a receiving point at the opposite corner of the plane  $z_r = 0$ . For instance, a path connecting the point  $(x_s, y_s) = (X_s/2, Y_s/2)$  in the source plane to the point  $(x_r, y_r, z_r) = (-X_r/2, -Y_r/2, 0)$  in the receiving space, as depicted in Fig. S1(a). Therefore, setting the right side of Eq. (S15) to be smaller than  $\lambda/2$ , leads to the following condition for the spacing distances  $d_x$  and  $d_y$ :

$$d_x = d_y < \frac{2}{\sqrt{2}} \frac{\lambda/2}{\sin \theta_{\text{max}}} = \frac{2\lambda}{\sqrt{2}} \frac{\sqrt{(X_s + X_r)^2/4 + (Y_s + Y_r)^2/4 + L^2}}{Y_s + Y_r}. \quad (\text{S17})$$

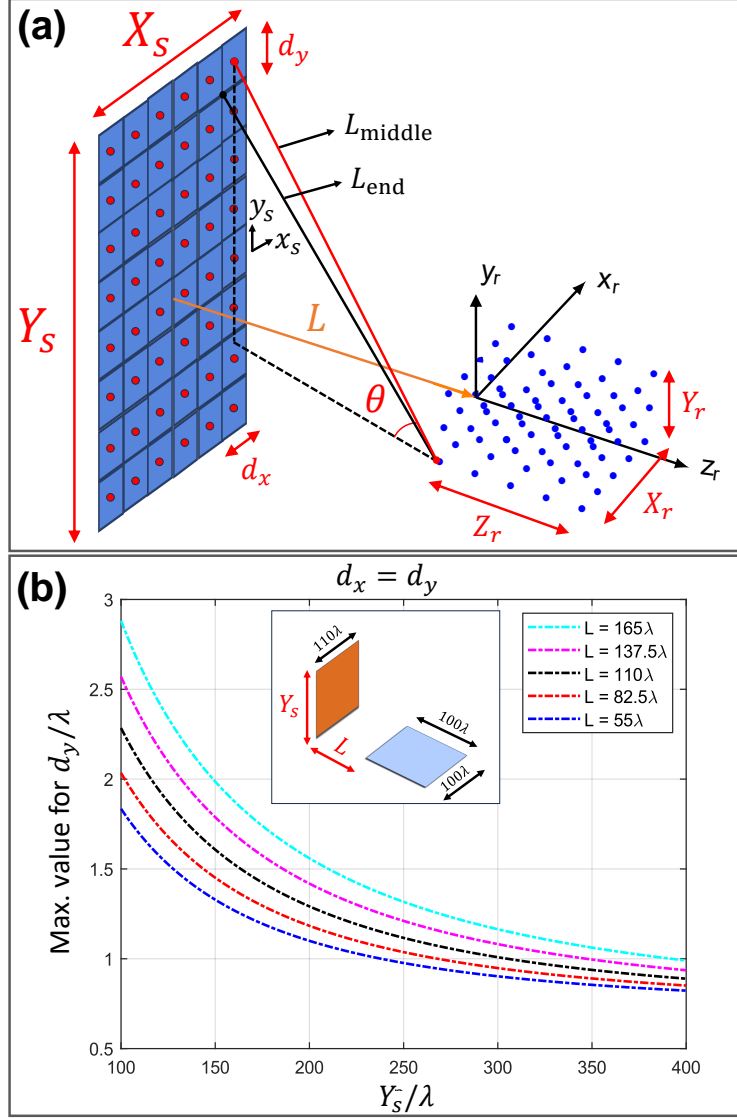


**Figure S1: Estimating an upper limit value to the spacing distances between the source points.** (a) Schematic showing the array of source points spaced from each other by  $d_x$  and  $d_y$ . The collection of the source points (red dots) must behave essentially as a set of uniform source patches (blue squares) covering the entire source plane. For a given receiving point and source patch, we compute the difference between two path lengths: one connecting the middle of the patch  $L_{\text{middle}}$  (in red) and another one connecting one of the corners of the patch  $L_{\text{corner}}$  (in black). Setting this difference to be less than half a wavelength, we can assume that the resulting wave amplitude created by a point source (in the middle of the patch) at the receiving point is approximately equal to the one created by the patch. (b) Maximum allowed values for  $d_x = d_y$  for the source and receiving space of Fig. 1(b) - a single horizontal plane - as function of the number of source points along the  $y_s$  direction and for different values of the on-axis longitudinal separation distance  $L$  between the spaces.

For the source and receiving spaces of Fig. 1(a) of the main text, parameterized according to Table 1, in which we adopted  $d_x = d_y = \lambda$ , Eq. (S17) yields  $d_x = d_y < 1.20\lambda$ . If we increase the number of source points along the  $y_s$  direction to  $p_y = 311$  (resulting in  $Y_s = 310\lambda$ ), the criterion of Eq. (S17) yields  $d_x = d_y < 0.991\lambda$ , implying that the source points at the top and bottom  $y_s$  positions no longer behave as uniform source patches. To solve this issue, we must consider a denser array of source points ( $d_x = d_y < \lambda$ ) for those aperture regions. In Fig. S1(b) we show the maximum allowed value of  $d_y$  for different values of  $Y_s$  and  $L$ . Notice that as we move to source points located at higher  $y_s$  positions (i.e., away from the aperture center  $y_s = 0$ ), progressively lower values for the spacing distance  $d_x$  and  $d_y$  are demanded. Additionally, reducing the on-axis longitudinal separation distance  $L$  between the spaces also imposes lower values for these spacing distances.

For a set of receiving horizontal planes, such as the set of 10 uniformly spaced ones analyzed in Fig. 4 in the main text, the criterion of Eq. (S17) is more restrictive for the spacing distances  $d_x$  and  $d_y$  compared to a single horizontal since the transverse dimension of the receiving  $Y_r$  is no longer null. For the example shown in the main text and parameterized accordingly to Table 1, in which we adopted  $d_x = d_y = 0.5\lambda$ , Eq. (S17) yields  $d_x = d_y < 0.789\lambda$ .

## Supplementary Note 4: Coupling strengths and intensity profiles of communication modes

**Receiving points distributed in a horizontal plane** In this source-receiving-space configuration, the coupling strength curve is characterized by a series of steps. As we clarify below, the number of strongly coupled steps corresponds to the number  $N_z$  of effective longitudinal ( $z_r$  direction) modes supported by the configuration. Meanwhile, the number of modes within each step corresponds approximately to the number of effective transverse modes. There are essentially two types of transverse modes in each step: strongly coupled and partially coupled modes. There will also be weakly coupled transverse modes associated with wave tunneling escape <sup>5</sup>, though these are so weak that they essentially do not show up in the main series of steps. The strongly coupled modes are those that couple strongly throughout the longitudinal length  $Z_r$  of the receiving space, and their coupling strengths correspond to the nearly flat region of the step. In contrast, partially coupled modes are modes that do not strongly couple all the way to the far end  $z_r = Z_r$  of the horizontal receiving plane, although they are able to couple relatively well at least into some fraction of the receiving space at the end closest to the source  $z_r = 0$ . These partially coupled modes give rise to the moderately steep fall-off in the coupling strength curve after the last strongly coupled mode on a given step. The number of strong effective transverse modes  $N_{x,\text{str}}$  and the number of effective longitudinal modes  $N_z$  can be computed as the maximum number of intensity fringes we can form in the receiving horizontal plane along its entire transverse  $X_r$  and longitudinal  $Z_r$  dimensions, respectively, as illustrated in Figs S2(a-b). For  $N_{x,\text{str}}$ , we compute the number of intensity fringes at the final longitudinal position ( $z_s = L + Z_r$ ) of the receiving space created by the two furthest source points along the source  $x_s$  transverse direction, i.e. with a spacing distance equal to the lateral extent  $X_s$  of the source plane. Since we can reasonably consider that  $X_s$  is significantly smaller than the longitudinal distance  $L + Z_r$ , we can use the one-dimensional paraxial heuristic number, defined in Ref. 1, which evaluates the number of effective modes in the case of transverse source and receiver lines. Thus, in our case,  $N_{x,\text{str}}$  is evaluated as:

$$N_{x,\text{str}} = \frac{X_r X_s}{(L + Z_r)\lambda}. \quad (\text{S18})$$

To evaluate the number  $N_z$  of effective longitudinal modes, we assume an off-axis source point at the vertical position  $y_s = Y_s/2$  and one at the origin  $y_s = 0$  [points A and O in Fig. S2 (b)] and compute the difference in path length between the waves from these points at the initial  $z_s = L$  and final  $z_s = L + Z_r$  longitudinal positions of the receiving plane [points  $P_L$  and  $P_R$  in Fig. S2(b)]. At point  $P_L$ , this difference is  $l_L = r_L - z_L = \sqrt{(Y_s/2)^2 + L^2} - L$  while at point  $P_R$ ,

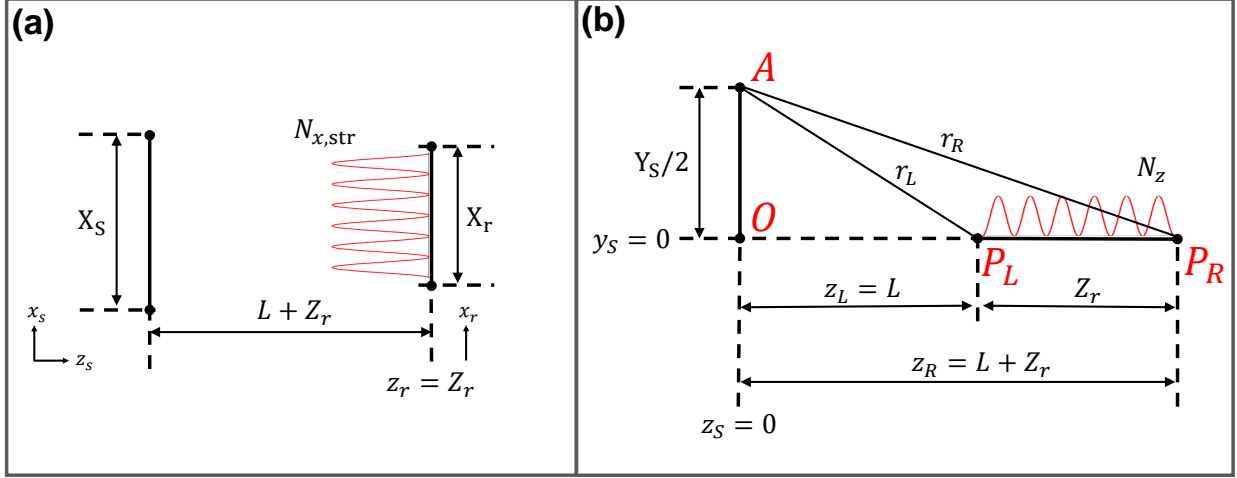


**Figure S2: Number of effective modes in a transverse source plane and a horizontal receiving plane configuration.** (a) Schematic to determine the number of effective strong transverse modes  $N_{x, \text{str}}$  as the maximum number of intensity fringes we can form along the transverse width  $X_r$  of the receiving plane at the end of its longitudinal length ( $z_r = Z_r$ ). (b) Similarly, the number of effective longitudinal modes  $N_z$  is determined as the maximum number of intensity fringes we can form along the receiving longitudinal distance  $Z_r$ .

$l_R = r_R - z_R = \sqrt{(Y_s/2)^2 + (L + Z_r)^2} - (L + Z_r)$ . Thus, as we proceed from point  $P_L$  to  $P_R$  we pass through a number  $N_z$  of complete interference fringes along the  $z_r$  direction given by:

$$N_z = \frac{l_L - l_R}{\lambda} = \left( \sqrt{(Y_s/2)^2 + L^2} - \sqrt{(Y_s/2)^2 + (L + Z_r)^2} + Z_r \right) \frac{1}{\lambda}, \quad (\text{S19})$$

for any particular fixed phases of the point sources at A and O. If we imagine that we moved the off-axis source progressively from point O to point A, we could therefore progressively change the number of fringes  $N_z$ , and along the way, we could imagine that we could create approximately different fringe patterns, with different numbers of periods, that are orthogonal to one another. From Eq. (S19) we can also compute the vertical source distance  $Y_{n_z}$  required to generate a particular number  $n_z$  of longitudinal fringes. Replacing  $Y_s/2$  by  $Y_{n_z}$  and  $N_z$  by  $n_z$  in Eq. (S19) leads to:

$$Y_{n_z}/\lambda = \pm \frac{\sqrt{n_z[2(Z_r/\lambda) - n_z][4L(L + Z_r)/\lambda^2 + 2(Z_r/\lambda)n_z - n_z^2]}}{2[(Z_r/\lambda) - n_z]}. \quad (\text{S20})$$

In view of Eq. (S20), we can categorize the modes according to their behavior along the

vertical source dimension, setting  $Y_{n_z}$  as a characteristic parameter. For the modes within the first step ( $n_z = 1$ ),  $Y_1$  corresponds to the extent in the  $y_s$  direction (relative to the center) of the intensity profiles of the source eigenfunctions. Meanwhile, for higher steps,  $1 < n_z \leq N_z$ ,  $Y_{n_z}$  corresponds to the vertical positions  $y_s = \pm Y_{n_z}$  where the source eigenfunction profiles are centered. To illustrate this, in Supplementary Video 1, we show the intensity profiles of all the first 250 well-coupled communication modes of the configuration parametrized as listed in Table 1. The coupling strengths of this configuration are shown in Fig. S3 (a), in which the vertical dashed lines highlight the last strong mode of each step and the inset sub-figure depicts the absolute values of  $Y_{n_z}$  computed from Eq. (S20). The strong modes of the first step correspond to the interval  $1 \leq j \leq 52$ , thus totaling a number of  $N_{x,\text{str}} = 52$  effective transverse modes, as predicted by Eq. (S18). Past these modes, we next find the partially coupled modes before we arrive at the strongly coupled modes of the near-flat region of the next step. In Fig. S3(b), we show the normalized intensity profiles of the last four strong modes ( $j = 49, \dots, 52$ ) and the first two partially coupled modes ( $j = 53, 54$ ) of the first step. As we move from one step to another, the source eigenfunction profiles progressively occupy higher vertical positions  $y_s = \pm Y_{n_z}$ , as predicted by Eq. (S20). As a result, their receiving eigenfunction profiles acquire an additional fringe along the  $z_r$  direction, thus providing progressively higher longitudinal spatial frequencies. This is illustrated in Fig. S3(c) in which we show the intensity profile of the last strong communication mode of the steps  $n_z = \{4, 8, 12, 14, 16, 18\}$ . Notice that as the vertical positions  $y_s = \pm Y_{n_z}$  approach the edges  $y_s = \pm Y_s/2$  of the source plane, more of the intensity profile of the source eigenfunction is compressed near these upper and lower edges of the finite source aperture. Associated with this compression, the receiving eigenfunction is no longer able to couple as strongly as the ones of the first steps throughout the entire length of the receiving space, as depicted in Fig. S3(d). For the purposes of discussion, we will still refer to these modes of the final steps as "strong" modes. Essentially, for these final steps, since their nominal values  $|Y_{n_z}|$ , given by Eq. (S20), approach the actual size of the source aperture ( $Y_s/2$ ), they are very close to passing the conventional diffraction limit for forming beams at the far end of the receiving space.

After the series of steps of up to  $n_z = 18$ , the singular values show a rapid fall-off decrease in their magnitude, as noted at the end of the coupling strength curve in Fig. S3(a) and also in Fig. S4 in which we show this coupling strength curve up to the first 1400 modes on a logarithmic scale. This ultimate rapid fall-off is a universal behavior in the analysis of communication modes, regardless of the shape of the receiving and source spaces<sup>1</sup>. Recently, this behavior has been explained as a consequence of the tunneling escape of waves from any arbitrary finite source volume

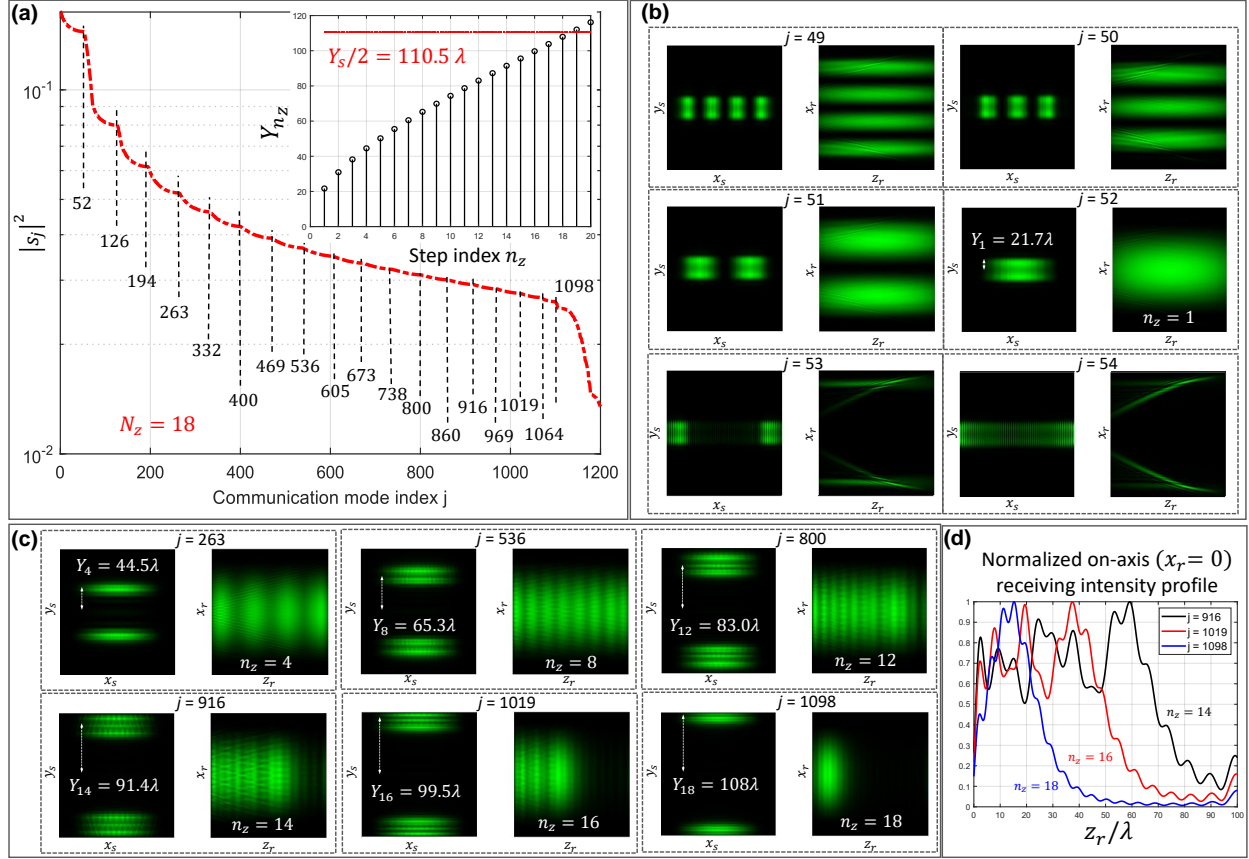


**Figure S3: Communication modes and their coupling strengths associated with a transverse source plane and a horizontal receiving plane. (a)** Coupling strengths on a logarithmic scale and in order of decreasing size of their magnitude of the first 1200 modes for this configuration parameterized as listed on Table 1. The vertical dashed lines highlight the last strong mode of each step and the inset sub-figure depicts the characteristic vertical position  $Y_{n_z}$  of the source eigenfunctions of each step. Normalized squared amplitude of: **(b)** the last four strong modes and the first two partially coupled modes of the first step  $n_z = 1$ , **(c)** the last strong mode of the steps  $n_z = \{4, 8, 12, 14, 16, 18\}$ . **(d)** Normalized on-axis intensity profile along the receiving longitudinal distance for the last strong mode of the steps  $n_z = \{14, 16, 18\}$ .



<sup>5</sup>. By means of an analysis based on spherical waves, it has been shown that beyond a number of well-coupled modes, waves associated with subsequent modes must tunnel to escape the finite source volume. We expect that this transition from the propagating region to the tunneling escape region occurs precisely when the coupling strengths fall off rapidly. For our source-receiving configuration, the condition for the onset of tunneling escape of waves is essentially  $|Y_{n_z}| > Y_s/2$ , or equivalently,  $n_z > N_z$ . Figure S4 makes the clear point that, above some finite number of modes, the coupling strengths of subsequent modes drop rapidly, practically limiting the number of usable modes. As has been argued in Ref. 5, this kind of fall-off is inevitable.

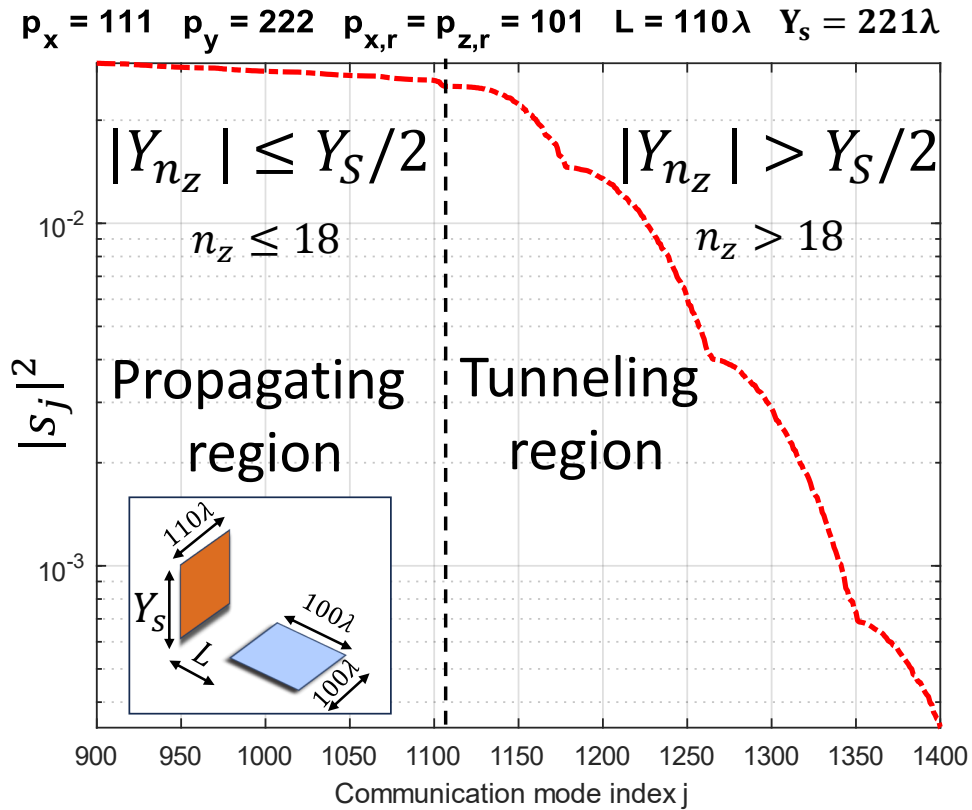


**Figure S4: Rapid fall-off decrease of the coupling strengths after the regions of well coupled modes (series of steps).** Coupling strengths on a logarithmic scale of the source-receiving system configuration parameterized as listed on Table 1. The rapid fall-off of the coupling strengths is a consequence of the tunneling escape of waves from any arbitrary finite source volume. For the source-receiving-space configuration of a transverse plane and a horizontal receiving plane, the condition for the onset of tunneling escape of waves is when the vertical positions of the source eigenfunction profiles become larger than the source aperture size  $|Y_{n_z}| > Y_s/2$ .

Equations (S18) and (S19) are useful to give us a sense of the total number of effective modes from the product  $N_{x,\text{str}}N_z$  before solving the SVD problem. This can only be a rough estimate because it does not count the partially coupled modes, particularly in the earlier steps, and in the later steps there may be not as many strongly coupled modes as in the first steps. This is illustrated in Fig. S5(a) which compares the coupling strengths for different values of the vertical dimension  $Y_s$  of the source plane and we highlight the indexes of the last strong mode of the blue curve (for  $Y_s = 166\lambda$ ). Furthermore, Fig. S5(a) clearly show that increasing the vertical dimension  $Y_s$  of the source substantially increases the number of useful modes.

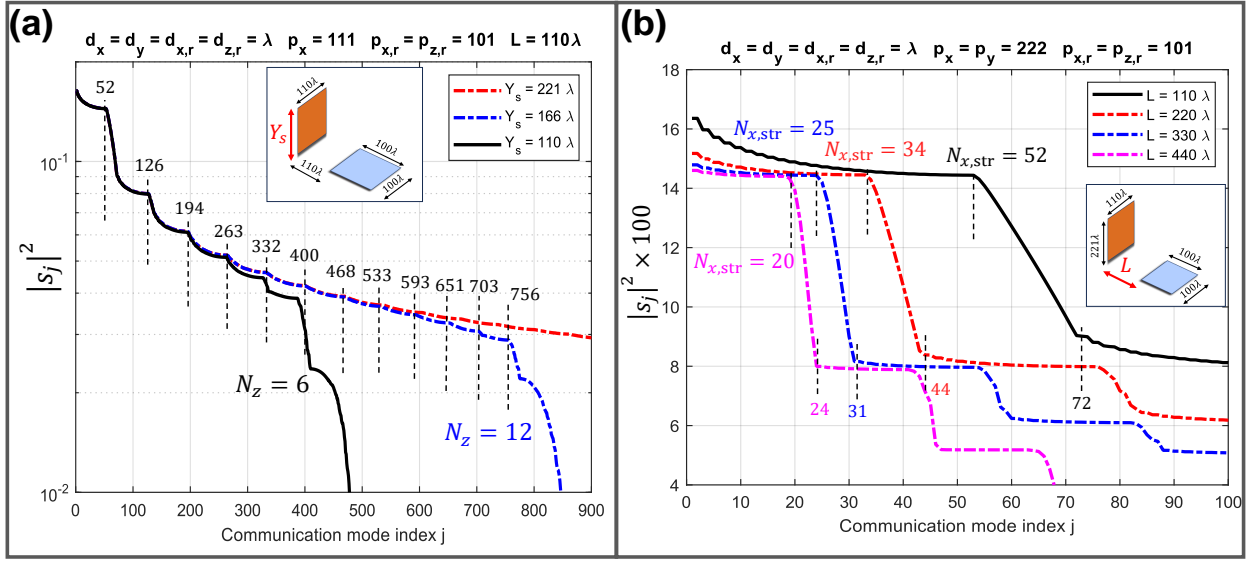


**Figure S5: Influence of the finite source aperture vertical dimension  $Y_s$  and the longitudinal distance  $L$  on the number of strong modes.** Coupling strengths of the source-receiving system configuration parameterized as listed on Table 1 for (a) different values of  $Y_s$  (on a logarithmic scale) and (b) for different values of  $L$ . In (a) the dashed vertical lines highlight the last strong mode of each step of the blue curve ( $Y_s = 166\lambda$ ). In (b) these lines highlight the last strong mode of the first step and the first strong mode of the second step. Increasing the source vertical dimension  $Y_s$  increases the number of effective longitudinal modes  $N_z$ , i.e., the number of steps in the coupling strength curve. Meanwhile, decreasing the longitudinal distances between the spaces also promotes an increase of the number of strong transverse modes and partially coupled modes in each step.

The number of strong transverse modes  $N_{x,\text{str}}$  in each step can be controlled by changing the longitudinal distance  $L$ . This is shown in Fig. S5(b) which depicts the coupling strengths for different values of  $L$ . The upper vertical dashed lines highlight the last strong mode of the first step while the bottom lines highlight the first strong mode of the second step. As we move far from

the paraxial limit, that is, by decreasing the longitudinal distance  $L$ , not only the number of strong transverse modes  $N_{x,\text{str}}$  increases but also the number of partially coupled modes  $N_{x,\text{part}}$ . In fact, for lower values of  $L$  we can even find partially strong modes from a previous step inside the region of strong modes of the next step. This is the case for  $L = 110\lambda$  (black curve) in which although the modes  $j = \{74, 79, 90, 92\}$  have coupling strengths smaller than that of the first strong mode of the second step ( $j = 72$ ), they are partially coupled modes of the first step (see Supplementary Video 1). Finally, as we approach the paraxial limit, we expect the number of partially coupled modes to follow:

$$N_{x,\text{part}} = \frac{X_r X_s}{L\lambda} - \frac{X_r X_s}{(L + Z_r)\lambda} = \frac{X_r X_s}{L\lambda} - N_{x,\text{str}}, \quad (\text{S21})$$

i.e., being evaluated as the difference between the number of intensity fringes at the near-longitudinal position of the receiving plane ( $z_r = 0$ ) and that at the end longitudinal position ( $z_r = Z_r$ ). For  $L = 440\lambda = 4X_s$  (magenta curve), Eq.( S21) yields  $N_{x,\text{part}} = 4$  which approaches the actual number of 3 partially coupled modes seen in this curve before its second step.

**Receiving space composed of a set of horizontal planes** The communication modes associated with this receiving space are closely related to the modes of a single horizontal plane. The substantial difference is that the additional degree of freedom afforded by the transverse direction  $y_r$  of the receiving space results in an increase in the number of modes. These additional modes have similar intensity profiles within all horizontal planes but with distinct amplitude profiles along the  $y_r$  direction. In Fig. S6(a), we show the coupling strengths  $|s_j|^2$  of the first 3500 modes, ordered by decreasing size of their magnitude, associated with the source and receiving configuration of Fig. 1(c) in the main text with the values of the parameters listed in Table 1. The normalized squared amplitude of the source and receiving eigenfunctions of the first 250 well-coupled modes are shown in Supplementary Video 2. We notice that we can identify groups of communication modes whose receiving eigenfunctions are characterized by the same intensity profile over all horizontal planes but modulated by distinct amplitude profiles along the  $y_r$  direction. To illustrate this phenomenon, in Fig. S6(b), we zoom-in the region of the coupling strength curve containing the first 70 well-coupled modes. From this figure, we identify groups of modes (highlighted by circles), each of which contains 16 modes. The modes of the first group ( $j = 1, \dots, 16$ ) have the same 'V' shaped intensity profile over the horizontal planes but with this profile modulated by distinct amplitudes along the  $y_r$  direction, as seen from the sub-figures of Fig. S6(c). Each sub-figure shows the source (on the left) and the receiving (on the right) eigenfunction intensity profiles of some of the modes within the first group ( $j = \{1, 3, 5, 7, 9, 16\}$ ). The other modes within this group are degenerate modes of these ones. Notice incidentally that the 'V' shaped intensity pro-

files of these modes are similar to the first mode  $j = 1$  associated with a single horizontal plane of receiving points shown in Fig. 2(c) in the main text. In fact, this similarity also applies to the other groups of modes. To illustrate this, the last two sub-figures of Fig. S6 show the source and receiving intensity profiles associated with the first mode of the second and third groups ( $j = 17$  and  $j = 33$ ). Notice that the intensity profiles of these modes over the horizontal planes are similar to the third  $j = 3$  and fifth  $j = 5$  modes for a single horizontal receiving plane, shown in Fig. 2(c) in the main text.

**Cylinder surface as a receiving space** In contrast to the communication modes for a receiving horizontal plane in which the source eigenfunctions are symmetric with respect to the  $y_s = 0$  axis, the source eigenfunctions associated with a cylindrical receiving surface either present rotational symmetries when their intensity profiles are rotated for some angles with respect to the optical axis, or we can find pairs of eigenfunctions that are related to each other by a rotation angle. In Fig. S7(a) we show the coupling strengths  $|s_j|^2$  of the first 1000 modes, ordered by decreasing the size of their magnitude, associated with the source and receiving configuration of Fig. 1(d) in the main text with the values of the parameters listed in Table 1. The normalized intensity profiles of the first two communication modes are shown in Fig. S7(b). Their source eigenfunctions, shown on the left of each sub-figure, are related to each other by a rotation of  $180^\circ$ . Incidentally, this symmetry also applies to their receiving eigenfunctions whose intensity profiles are shown in the receiving surface [in which  $\phi_r = \text{atan}(y_r/x_r)$  is the azimuth coordinate of the receiving rings] and at the mid transverse plane  $z_r = Z_r/2$  of the receiving space (plots on the middle and on the right in each sub-figure). Finally, similarly to the previous distributions, as we progressively move to modes with less coupling strength, their receiving eigenfunctions acquire progressively higher longitudinal spatial frequencies. This is depicted in Fig. S7(c) which shows the intensity profile of communication modes from different regions of the coupling strength curve of Fig. S7(a) as highlighted by the arrows. In particular, the intensity profile of their receiving eigenfunctions consists of four straight spots extending along the entire receiving longitudinal distance and angularly spaced  $90^\circ$  from each other. The difference between these profiles is that they acquire progressively a large number of regions of maximum intensity along the longitudinal  $z_r$  direction. The intensity profiles of all the first 100 well-coupled communication modes are shown in Supplementary Video 3.

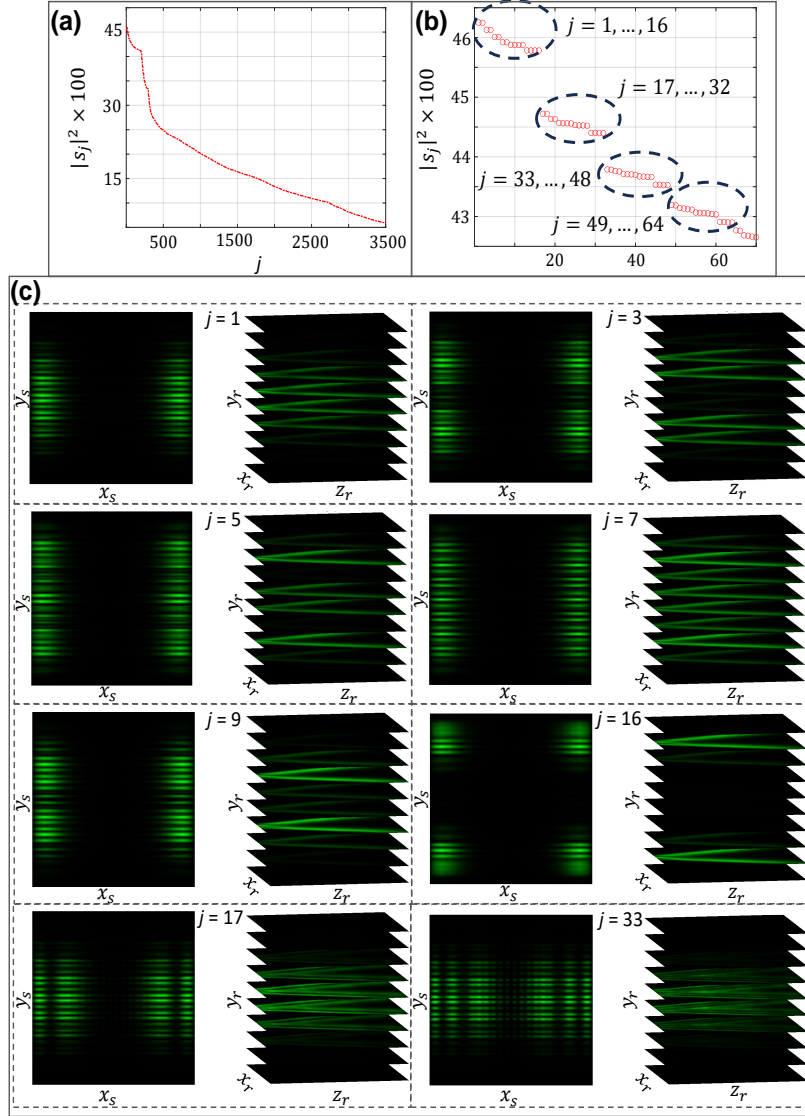


**Figure S6: Communication modes and their coupling strengths associated with a transverse source plane and a set of uniformly spaced horizontal receiving planes. (a)** Coupling strengths  $|s_j|^2$  of the first 3500 communication modes, ordered by decreasing size of their magnitude, associated with the configuration of Fig. 1(c), parameterized as listed on Table 1. **(b)** A zoom-in visualization of the coupling strengths of the first 70 well-coupled modes. Each highlighted group of modes is characterized by having their receiving eigenfunctions built from the same intensity profile over the  $x_r z_r$  plane but modulated by distinct amplitude profiles along the  $y_r$  direction. **(c)** Normalized intensity profile of the source (on the left of each sub-figure) and receiving (on the right of each sub-figure) eigenfunctions of the communication modes  $j = \{1, 3, 5, 7, 9, 16\}$ , which belongs to the first highlighted group of modes. The other modes within this first group are degenerate modes of these ones. The two last sub-figures show the source and eigenfunctions of the first mode of the two subsequent groups ( $j = 17$  and  $j = 33$ ).

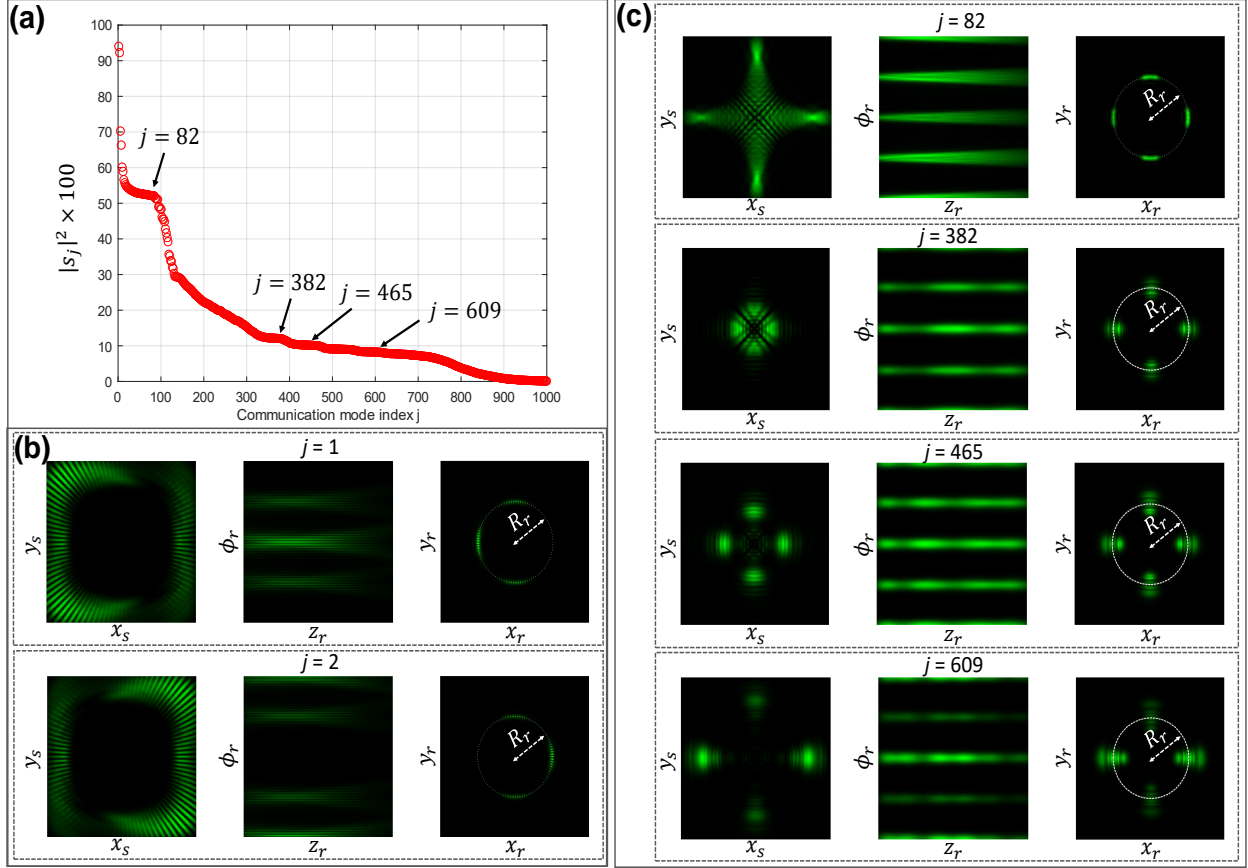


**Figure S7: Communication modes and their coupling strengths associated with a transverse source plane and a curved receiving space in which the receiving points are arranged over the longitudinal surface of a cylinder. (a)** Coupling strengths in order of decreasing size of their magnitude of the first 1000 modes for this source-receiving system configuration parameterized as listed in Table 1. **(b-c)** Normalized intensity profiles of first two communication modes and of the modes highlighted by the arrows in (a). From left to right in each sub-figure: source eigenfunction in the source plane, receiving eigenfunction over the lateral cylindrical surface in terms of its azimuth angle and the longitudinal coordinate  $z_r$ , and at the mid transverse plane of the receiving space ( $z_r = Z_r/2$ ). In all the sub-figures,  $R_r$  refers to the radius of the cylindrical surface.

## Supplementary Note 5: Characteristic minimum longitudinal length of wave field generated by a finite source transverse plane

In this section, we derive the characteristic minimum length of wave field  $\Delta z$  our transverse source plane can create along the propagation direction at a particular receiving point  $P_0$  located at  $(x_r, y_r, z_r) = (x_{r,0}, y_{r,0}, z_{r,0})$ . This point  $P_0$  is located at a longitudinal distance  $z_s = z_0 = L + z_{r,0}$  from the source plane origin, as illustrated in Fig. S8(a). Additionally, assume that  $\Delta Y$  is the extent of the source intensity profile from the position  $y_s = y_{r,0}$ , connecting a source point that is aligned with the receiving plane (point O) to the furthest triggered source point located at point A in the source plane. Our derivation is based on the assumption that the waves created by these two source points interfere constructively at the point  $P_0$ , resulting in a maximum intensity at this point. At the same time, these waves interfere destructively at points  $P_L$  and  $P_R$  located on either side of  $P_0$  as shown in Fig. S8(a). Therefore, an estimation of the minimum length of wave field  $\Delta z$  our source aperture is able to create at position  $z_0$  corresponds to the separation distance between the points  $P_L$  and  $P_R$ :

$$\Delta z = (z_0 - z_L) + (z_R - z_0) = \Delta z_L + \Delta z_R. \quad (\text{S22})$$

At the points  $P_L$  and  $P_R$  we must have a half a wavelength ( $\lambda/2$ ) difference for the relative path length between the waves from point O and from point A compared to that at point  $P_0$ . Since the distances from point A to all the three points  $P_0$ ,  $P_L$  and  $P_R$  are given by:

$$r_0 = \sqrt{(z_0)^2 + (\Delta Y)^2}, \quad (\text{S23a})$$

$$r_L = \sqrt{(z_0 - \Delta z_L)^2 + (\Delta Y)^2}, \quad (\text{S23b})$$

$$r_R = \sqrt{(z_0 + \Delta z_R)^2 + (\Delta Y)^2}, \quad (\text{S23c})$$

and the distances from point O to these points are respectively  $z_0$ ,  $z_L = z_0 - \Delta z_L$  and  $z_R = z_0 + \Delta z_R$ , computing the relative path lengths for each of the points  $P_L$  and  $P_R$  with respect to that of point  $P_0$  leads to:

$$\Delta s_L = (r_L - z_L) - (r_0 - z_0) = r_L - r_0 + \Delta z_L, \quad (\text{S24a})$$

$$\Delta s_R = (r_0 - z_0) - (r_R - z_R) = r_0 - r_R + \Delta z_R. \quad (\text{S24b})$$

Thus, setting  $\Delta s_L = \Delta s_R = \lambda/2$ , we find a set of two equations, one for  $\Delta z_L$  and another one for  $\Delta z_R$ :

$$\sqrt{(z_0 - \Delta z_L)^2 + (\Delta Y)^2} - \sqrt{(z_0)^2 + (\Delta Y)^2} + \Delta z_L = \lambda/2, \quad (\text{S25a})$$

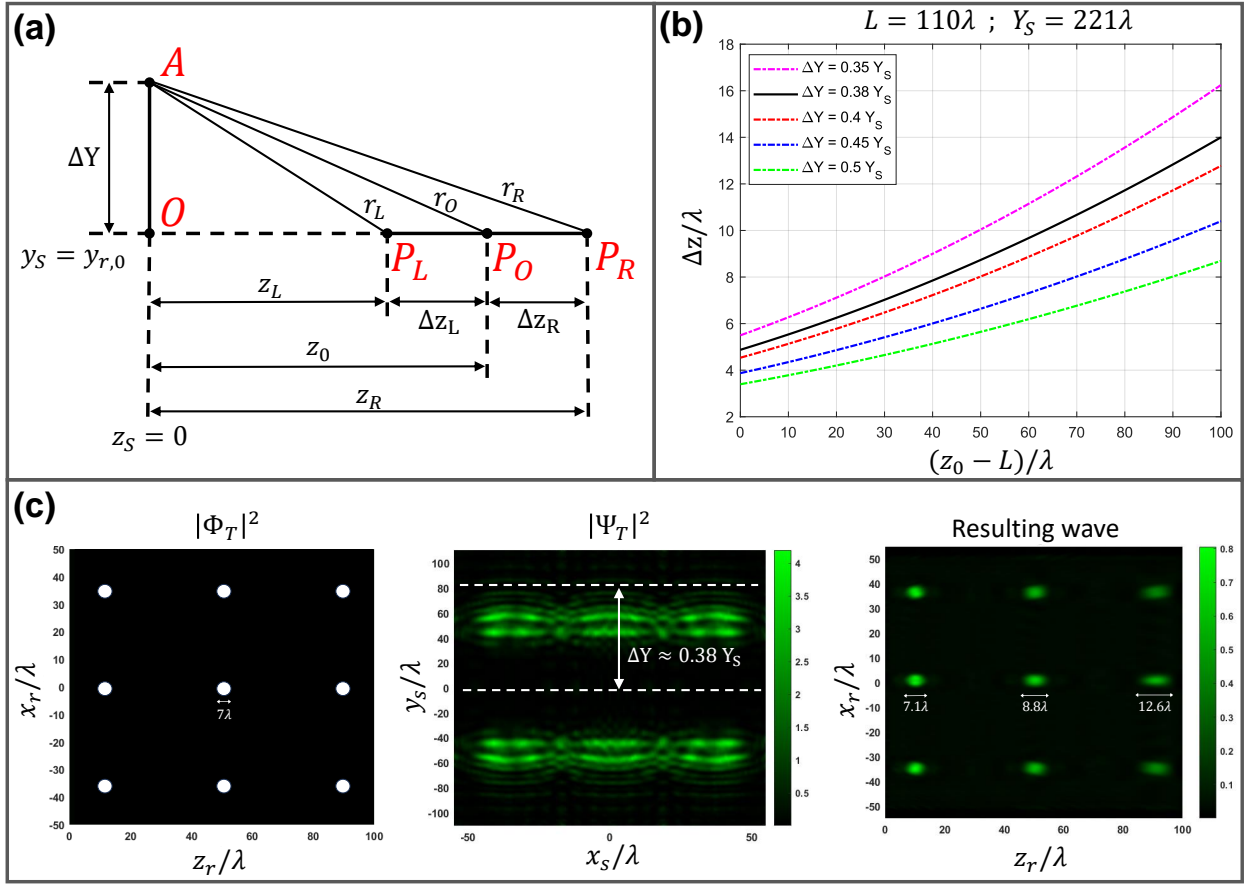


**Figure S8: Estimating the characteristic minimum length of wave field our finite transverse source aperture can create along the propagation direction.** (a) Schematic in which a point  $P_0$ , for which we estimate characteristic minimum length of wave field, is located at a position  $z_s = z_0$  from the source aperture and at a receiving horizontal plane with  $y_r = y_{r,0}$ . We assume that the source field extends for a distance  $\Delta Y$  from the  $y_s = y_{r,0}$  plane, from a point  $O$  to a point  $A$ . The minimum length of wave field  $\Delta z = \Delta z_L + \Delta z_R$  is assigned as the distance between points  $P_L$  and  $P_R$  located on either side of  $P_0$  and is computed by presuming that the waves coming from points  $A$  and  $O$  interfere constructively at the point  $P_0$  while they interfere destructively at the points  $P_L$  and  $P_R$ . (b) Values of  $\Delta z$  as function of the receiving plane  $z$  position and for distinct  $\Delta Y$  values. We assume the source and receiving space configuration shown in Fig. 1(b) and parameterized as listed on Table 1, i.e., a single horizontal plane with  $y_{r,0} = 0$ . (c) A simulation example involving the reconstruction of a target profile that consists of  $7\lambda$  diameter circles placed at distinct longitudinal positions along the receiving plane. We are only able to resolve the circles located at  $z_r = 10\lambda$  (the ones close to the source plane), as  $\Delta z < 7\lambda$  at this position and  $\Delta z > 7\lambda$  at the other  $z_r$  positions ( $z_r = 50\lambda$  and  $z_r = 90\lambda$ ).



$$\sqrt{(z_0)^2 + (\Delta Y)^2} - \sqrt{(z_0 + \Delta z_R)^2 + (\Delta Y)^2} + \Delta z_R = \lambda/2, \quad (\text{S25b})$$

which can be solved graphically or numerically for given values of  $z_0$  and  $\Delta Y$ . By solving for  $\Delta z_L$  and  $\Delta z_R$  from Eqs S25 (a-b), we sum these contributions up to compute the characteristic minimum length of wave field  $\Delta z$ , as in Eq. (S22). Values of  $\Delta z$  are shown in Fig. S8(b) as function of  $z_0$  and for distinct values of  $\Delta Y$ . Here we consider the source and receiving configuration shown in Fig. 2(a) in the main text, i.e., a single horizontal receiving space located at  $y_{r,0} = 0$ , in which the on-axis separation between the spaces is  $L = 110\lambda$  and the source plane has a total dimension of  $Y_s = 221\lambda$  along the  $y_s$  axis. Notice that  $\Delta z$  grows up quite rapidly with the distance  $z_r = z_0 - L$  within the receiving plane. Additionally, the extent  $\Delta Y$  of the source function is responsible not only for decreasing  $\Delta z$  but also its rate of change along the  $z$  direction. In Fig. S8(c) we provide a simulation example to demonstrate the fundamental limits imposed by our finite source aperture when we try to structure a spot with a longitudinal dimension smaller than  $\Delta z$ . Using the first  $M = 1200$  modes associated with the source and receiving configuration of Fig. 2(a) in the main text, we compute the required source function intensity  $|\Psi_T|^2$  and the resulting wave intensity at the horizontal receiving plane for a target profile consisting of  $7\lambda$  diameter circles centered at the following longitudinal positions along the receiving plane:  $z_r = 10\lambda$ ,  $z_r = 50\lambda$  and  $z_r = 90\lambda$ . While we are able to generate the circles located at  $z_r = 10\lambda$  relatively well, the resulting wave at the other circles' locations is characterized by spots with larger longitudinal dimensions, indicating that the values of the characteristic minimum length of wave field  $\Delta z$  at these locations are higher than the  $7\lambda$  longitudinal dimension of the target circles. In fact, their dimensions approximately satisfy the values of  $\Delta z$  given by the solid black curve of Fig. S8(b), computed for  $\Delta Y = 0.38Y_s$ , a value that matches with the extent of the source function intensity as depicted in Fig. S8(c).

For a receiving space that contains a set of parallel horizontal planes, a distinct maximum extent  $\Delta Y$  can be assigned to each horizontal plane  $y_r = y_{r,0}$  to compute the characteristic minimum length of wave field  $\Delta z$  at a certain longitudinal position  $z_r$  within each plane. Specifically, inner receiving planes can acquire higher values of  $\Delta Y$  compared to outer ones, as the maximum value we can assign to this parameter is  $\Delta Y = Y_s/2 - y_{r,0}$ . For this reason, it is expected that structuring small features at the outermost receiving planes is more challenging than at the inner ones. To illustrate this phenomenon, consider the receiving plane in which we projected the last ellipsoid slice (layer 8 in Fig. S10 located at  $y_{r,0} = 52.5\lambda$ ). Assuming  $\Delta Y = Y_s/2 - y_{r,0} = 75\lambda - 52.5\lambda = 22.5\lambda$ , i.e., the maximum value we can assign to this parameter for this plane, leads to  $\Delta z = 24.26\lambda$  at the center of that receiving plane ( $z_r = Z_r/2 = 25\lambda$ ). Because of this high value of  $\Delta z$  we are not able to completely resolve the last ellipsoid slice whose circle diameter is  $10\lambda$ .

From the analysis of the characteristic minimum longitudinal length of wave  $\Delta z$  provided in Fig. S8, we notice the importance of having a source function profile  $|\Psi_T|^2$  with as large an extent  $\Delta Y$  as possible to properly resolve a given target intensity profile along all the longitudinal distances  $z_r$  of the receiving space. To increase  $\Delta Y$  we must modulate the target profile with a phase front of the form  $\exp(iQz_r)$ , in which  $0 \leq Q \leq k = 2\pi/\lambda$ . In Fig. S9 we demonstrate how this phase front affects the source function profile and its corresponding resulting wave in the receiving space for different values of  $Q$ . As noticed, as we progressively decrease  $Q$ , more of the target profile content  $|a_j|$  falls onto the range of well-coupled modes ( $j \leq 1200$ ) of the receiving space set, giving rise to a resulting wave at the receiving plane that progressively resolves the target profile  $|\Phi_T|^2$ . For  $Q = 0.95k$ , the entire target profile falls onto the range of well-coupled modes and the target profile  $|\Phi_T|^2$  is fully resolved. Looking at the required source profile  $|\Psi_T|^2$ , the incorporation of the phase front  $\exp(iQz_r)$  has the effect of shifting  $|\Psi_T|^2$  away from the  $y_s = 0$  line. In view of that, the parameter  $Q$  can be associated with a cone angle  $\theta$  that the wave vector of the propagating wave from the source to the receiving space makes with the optical axis, such that  $Q = \cos(\theta)k$ . From this association, we can relate  $Q$  with the position along the  $y_s$  axis,  $y_s = \pm Y_T$ , around which the required source profile  $|\Psi_T|^2$  is localized. Assuming a ray that travels from the point  $(x_s, y_s) = (0, Y_T)$  at the source plane to the center of the receiving horizontal plane  $(x_r, z_r) = (0, Z_r/2)$  with an angle  $\theta$  with respect to the optical axis, it can be shown that  $Y_T = (L + Z_r/2) \tan[\cos^{-1}(Q/k)]$ . For  $Q = 0.975k$  [Fig. S9 (b)] and for  $Q = 0.95k$  [Fig. S9 (c)], this expression yields, respectively,  $Y_T = 36.46\lambda$  and  $Y_T = 52.59\lambda$ , which is in accordance with the vertical positions occupied by  $|\Psi_T|^2$  in Figs S9(b-c).

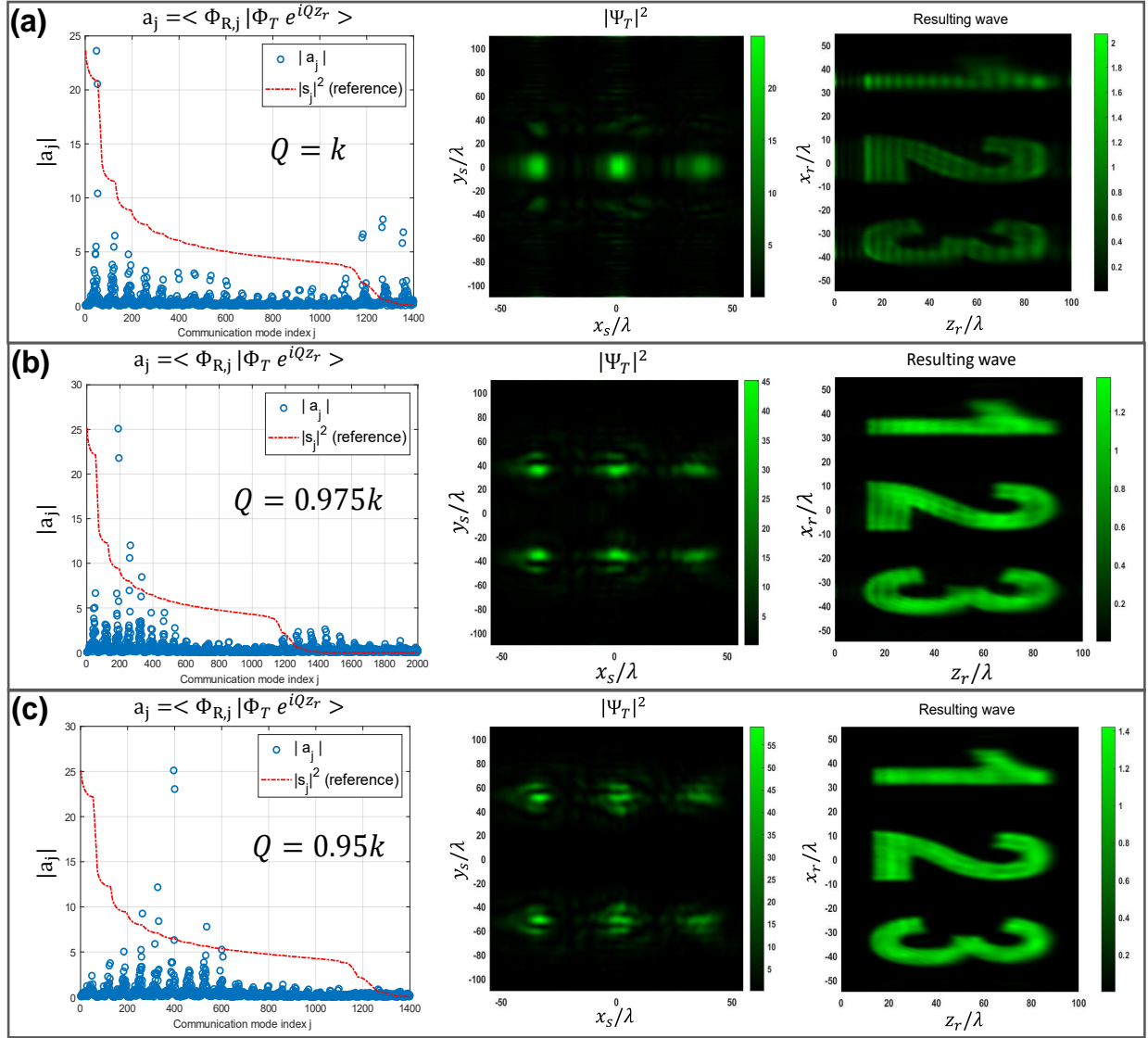


**Figure S9: Applying a phase front to project the entire target profile onto the range of well coupled modes.** Simulation example assuming the source and receiving space configuration of Fig. 1(a), parameterized as listed on Table 1 and the target profile  $\Phi_T$  of Fig. 2(b). We apply a phase front of the form  $\exp(iQz_r)$ , with  $0 \leq Q \leq k = 2\pi/\lambda$ , to project the target profile onto the receiving space set. Examples shown for (a)  $Q = k$ , (b)  $Q = 0.975k$  and (c)  $Q = 0.95k$ . For each sub-figure, from left to right: amplitude of the inner product coefficients between  $\Phi_T \exp(iQz_r)$  and the receiving eigenfunctions  $\{\Phi_{R,j}\}$  (blue circles) and the coupling strengths  $|s_j|^2$  of the communication modes (in red dashed line, in arbitrary units); corresponding required source function intensity profile at the source plane and its resulting wave in the receiving horizontal plane, computed using the first 1200 modes.

## Supplementary Note 6: Phase retrieval algorithm

Phase retrieval refers to a process of reconstructing a complex field by means of a phase-only platform. This process does not have a unique solution as the complex field can be encoded into a phase profile by many different approaches<sup>6,7</sup>. In this paper, we followed the approach developed in Ref. 8.

First we normalize the complex field of the resulting wave at the  $z = L$  transverse plane  $\phi(x_s, y_s, L)$  and write it in terms of an amplitude  $a(x_s, y_s)$  term, ranging from  $[-1, 1]$ , and a phase profile term  $b(x_s, y_s)$ , ranging from  $[-\pi, \pi]$ , as:

$$\phi_n(x_s, y_s, L) = a(x_s, y_s) \exp[i b(x_s, y_s)], \quad (\text{S26})$$

in which the sub-index  $n$  refers to the normalized complex field.

Next, we need to convert  $\phi_n(x_s, y_s, L)$  into a phase transmittance mask of the form:

$$h(x_s, y_s) = \exp[i\Phi(a, b)], \quad (\text{S27})$$

in which we omit the explicit dependence on the spatial coordinates  $(x_s, y_s)$  of the functions  $a$  and  $b$ , and  $\Phi$  is a phase modulation function. Our goal now is to establish a function  $\Phi$  that properly encodes the complex field  $\phi_n$ , incorporating amplitude variations as phase variations. To do this, we expand  $h(x_s, y_s)$  into a Fourier series in the domain of the phase profile  $b$  as follows:

$$h(x_s, y_s) = \sum_{q=-\infty}^{\infty} c_q^a \exp(iqb), \quad (\text{S28})$$

where the coefficients  $c_q^a$ , which depend on the amplitude profile  $a$ , are given by:

$$c_q^a = \frac{1}{2\pi} \int_{-\pi}^{\pi} \exp[i\Phi(a, b)] \exp(-iqb) db. \quad (\text{S29})$$

Notice from Eqs S28 and S29 that the complex field  $\phi_n(x_s, y_s, L)$  is fully recovered from the first order term ( $q = 1$ ) if we satisfy the following condition, usually referred as the encoding condition:

$$c_1^a = Aa, \quad (\text{S30})$$

for a given positive constant  $A$ . Based upon this condition, sufficient and necessary conditions for the function  $\Phi(a, b)$  can be obtained, resulting in:

$$\int_{-\pi}^{\pi} \sin[\Phi(a, b) - b]db = 0, \quad (\text{S31a})$$

$$\int_{-\pi}^{\pi} \cos[\Phi(a, b) - b]db = 2\pi Aa, \quad (\text{S31b})$$

which implies that the phase modulation function  $\Phi(a, b)$  must present an odd symmetry in the variable  $b$ . In this paper, we adopted the following  $\Phi$  function:

$$\Phi(a, b) = f(a) \sin(b), \quad (\text{S32})$$

that corresponds to the phase mask of type 3 proposed in Ref. 8. The factor  $f(a)$  in Eq. (S32) is obtained numerically from the encoding condition of Eq. (S30). Specifically, the corresponding Fourier coefficients for this phase modulation function, computed from Eq. (S29), are given by  $c_q^a = J_q[f(a)]$ , leading to the following encoding condition:

$$J_1[f(a)] = Aa. \quad (\text{S33})$$

We implemented a lookup table to numerically perform the Bessel function inversion in Eq. (S33). Choosing  $A = \max[J_1(\cdot)] = 0.5819$  leads to a function  $f(a)$  that acquires values over the interval  $0 \leq f(a) \leq 1.84$ . As a consequence, the phase domain of our phase mask  $h(x_s, y_s)$  is defined over the interval  $[-0.586\pi, 0.586\pi]$ , resulting in a total phase range of  $1.17\pi$ . For this phase range, our employed SLM can operate with a quantization of 800 gray levels.

Finally, we add a blazed grading with carrier spatial frequencies  $G_x$  and  $G_y$  to Eq. (S32). Thus, the phase mask that we encode onto the SLM is described by:

$$\Phi(a, b) = f(a) \sin[b + 2\pi(G_x x + G_y y)]. \quad (\text{S34})$$

## Supplementary Note 7: Aspect ratio of our reconstructed structured light waves

Because the SLM pixel pitch is much larger than the incident wavelength ( $\delta \approx 15\lambda$ ), the encoded phase mask occupies an area  $X_{\text{SLM}} \times Y_{\text{SLM}}$  within the SLM display significantly larger than our source space dimensions  $X_s \times Y_s$ . As a result of this scaling up process, the aspect ratio between the transverse and longitudinal dimensions of our measured light field does not follow the original 1:1 aspect ratio of our original (simulated) resulting wave within the receiving space. This stems from the fact that a magnification  $M$  of the light field's transverse dimensions leads to a magnification  $M^2$  of its longitudinal dimension. For further details, see Ref. <sup>9</sup>. In our implementation, the complex field  $\phi(x_s, y_s, L)$  was computed for  $x_s$  and  $y_s$  ranging from  $[-Y_s/2, Y_s/2]$  and we assigned a  $600 \times 600$  grid points in the SLM display to encode the phase mask, leading to a magnification of  $M_{\text{SLM}} = Y_{\text{SLM}}/Y_s = 9007.5\lambda/Y_s$ . Additionally, our  $4f$  system also alters the SLM out-going beam by a de-magnification of  $M_{4f} = f_2/f_1 = 3/4$ . Therefore, taking as an example the source and receiving space configuration of Fig. 2(a) in the main text in which  $Y_s = 221\lambda$  and the receiving horizontal plane has dimensions  $X_r = Z_r = 100\lambda$ , the reconstructed resulting wave extends for a transverse distance of  $M_{\text{SLM}}M_{4f}X_r = (40.76)(3/4)X_r = 3057\lambda$  and for a longitudinal distance  $M_{\text{SLM}}^2M_{4f}^2Z_r = 93443\lambda$ , leading to an aspect ratio of 1:30.57. To achieve an aspect ratio of 1:1, we need to satisfy the condition  $M_{4f}M_{\text{SLM}} = 1$ . For the configuration of Fig. 2(a), in which  $Y_s = 221\lambda$ , it leads to a de-magnification of  $M_{4f} = 1/40.76 = 0.0245$  for the  $4f$  system which could be implemented with  $f_1 = 400$  mm and  $f_2 \approx 10$  mm.

## Supplementary Note 8: Projecting an ellipsoid

Here we consider another target 3D light distribution to be projected onto the eight inner horizontal receiving planes of the distribution shown in Fig. 1(c). Specifically, we project eight layers of an ellipsoid, centered at the middle of the receiving volume  $(x_r, y_r, z_r) = (0, 0, Z_r/2)$  and whose semi-axes have lengths  $a = 0.4X_r = 20\lambda$ ,  $b = 0.4Y_r = 54\lambda$  and  $c = 0.4Z_r = 20\lambda$ . The intensity of the target receiving profile  $|\Phi_T|^2$  and of the required source function  $|\Psi_T|^2$  are shown in Fig. S10(a). The optical reconstruction and its transverse planes at  $z_r = Z_r/2$  and at  $z_r = Z_r/4$  are shown in Fig. S10(b) while in Fig. S10(c) we present measured and simulated results of the four bottom layers. Notice that we have a good reconstruction for all the layers except the last one (layer 8) in which the resulting wave is not able to structure a circle nor to achieve the same intensity as the other layers. The reason for this is because the target circle we assigned to this layer has a diameter smaller than the characteristic minimum spot  $\Delta z$  our source transverse plane is capable of resolving (see Supplementary Note 5). To fully resolve the circle of this layer, we need to consider a source plane with a larger dimension along the  $y_s$  axis (large  $Y_s$  value and potentially with smaller spacing distances  $d_x$  and  $d_y$  for the additional source points), allowing us to incorporate a phase front  $\exp(iQz_r)$  with a smaller value of  $Q$ , resulting in a source function with a higher extent  $\Delta Y$  along the  $y_s$  axis, thus leading to a smaller value for  $\Delta z$ .

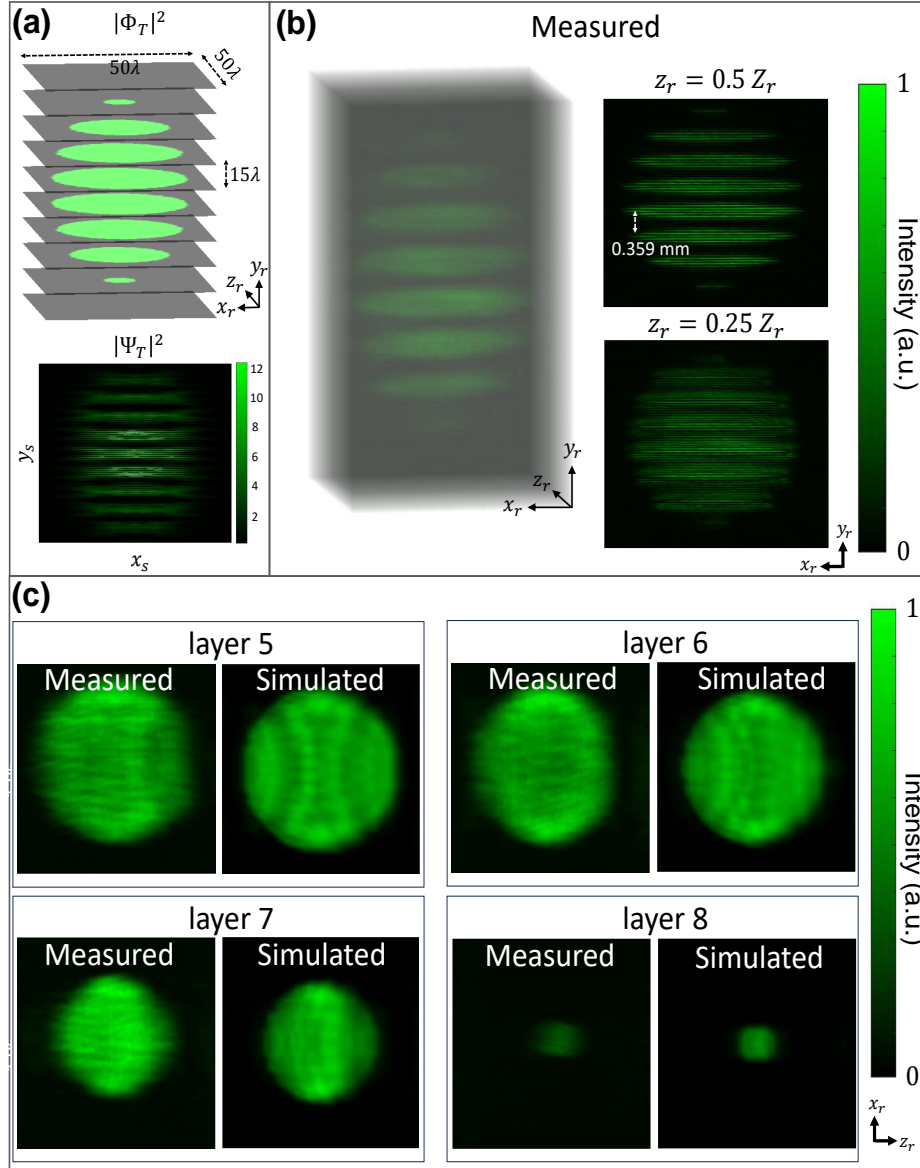


**Figure S10: Projecting eight layers of an ellipsoid.** (a) An ellipsoid with dimensions  $20\lambda \times 54\lambda \times 20\lambda$  is Projected over the eight inner horizontal receiving planes of the source-receiving space system of Fig. 1(c), parameterized as listed on Table 1. The resulting wave is computed using the first 3500 modes. (a) Target receiving intensity profile  $|\Phi_T|^2$  and its corresponding required source function intensity profile  $|\Psi_T|^2$ . (b) Optical reconstruction of the resulting wave using a phase-only SLM within a volume containing the receiving horizontal planes and at transverse planes located at the mid and quarter longitudinal distances,  $z_r = Z_r/2$  and  $z_r = Z_r/4$  ( $Z_r$ : longitudinal length of the planes). (c) Comparison between measured and simulated results for the four bottom ellipsoid layers.



## Supplementary Note 9: Reducing the separation distance between the horizontal receiving planes

In this section we apply our wavefront shaping method to a set of horizontal receiving planes with a tight separation distance between them. Specifically, we reduce the separation distance between the receiving horizontal planes analyzed in Fig. 4 in the main text from  $d_{y,r} = 15\lambda$  to  $d_{y,r} = 8\lambda$  and project the same eight digits onto the eight inner planes, as depicted in Fig. S11(a). Keeping the same phase front  $\exp(iQz_r)$  with  $Q = 0.95k$  to modulate the target profile and using first the  $M = 3500$  modes, the simulated resulting wave, shown in Fig. S11(b), is characterized by a cross-talk that deteriorates the reconstructed intensity profiles of the digits, as seen in Fig. S11(d). To remove this cross-talk while keeping the same separation distance  $d_{y,r} = 8\lambda$ , we need to reduce the ability of the source function to create high longitudinal spatial frequencies by increasing the parameter  $Q$  as exemplified in Fig. S11(c), in which the simulated resulting wave was computed for  $Q = 0.975k$ . As noticed from the reconstructed intensity profiles of the digits in Fig. S11(d), for a set of horizontal receiving planes separated by tight spacing distances, we must lose axial resolution to achieve intensity profiles with no cross talk.

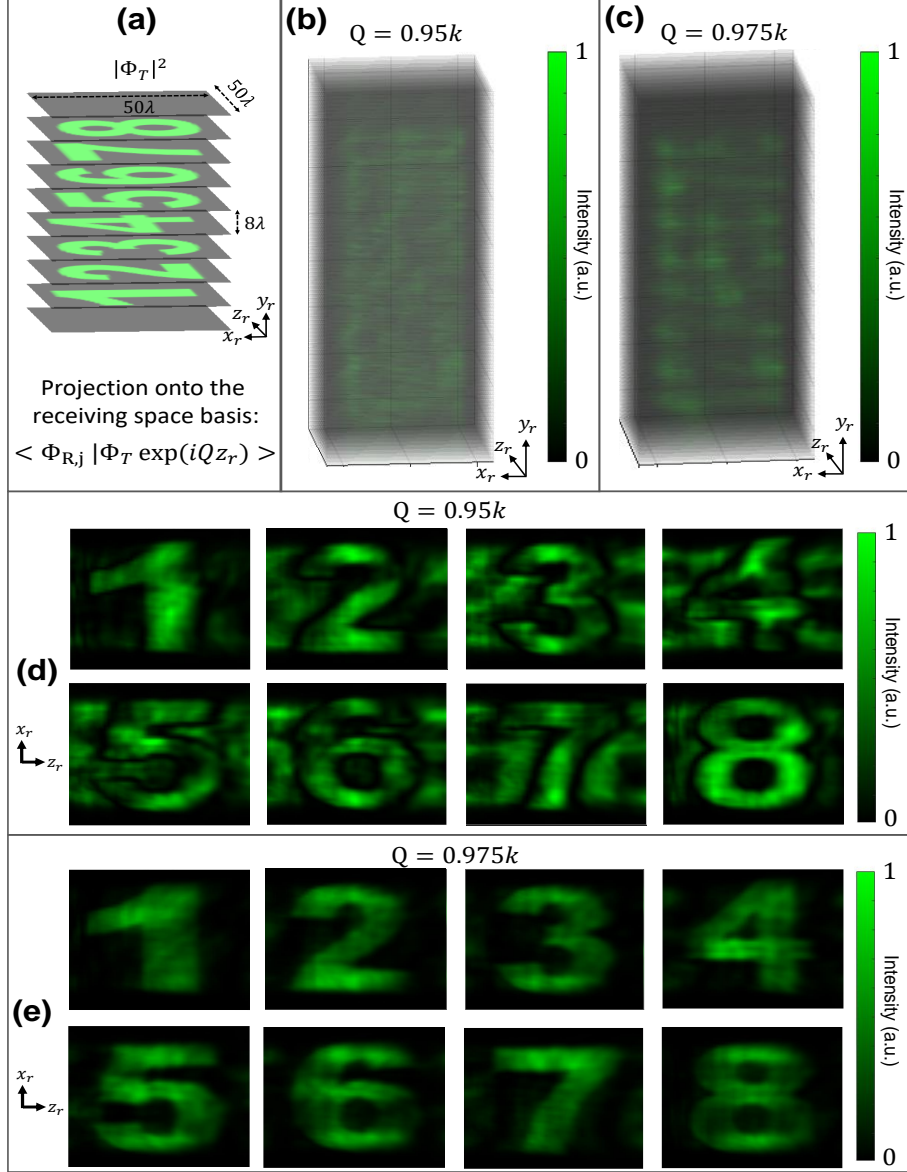


**Figure S11: Reducing the spacing distance between the receiving horizontal planes.** We consider the source-receiving space system of Fig. 1(c) parameterized accordingly to Table 1 except that the spacing between the horizontal receiving planes is reduced to  $d_{y,r} = 8\lambda$ . Similarly to the example of Fig. 4, we project eight digits within the eight inner horizontal receiving planes, modulate the target profile with a phase front  $\exp(iQz_r)$  and compute the resulting wave using the first 3500 modes. (a) Target intensity profile. (b) Simulated resulting wave within a volume containing the receiving horizontal planes and (d) within all the eight inner horizontal receiving planes for  $Q = 0.95k$ . (c) and (e) similar for  $Q = 0.975k$ . Notice that we must lose axial resolution (by adopting a higher value of  $Q$ ) to achieve intensity profiles with no cross-talk within tight separated horizontal receiving planes.

## Supplementary Note 10: Projecting structured light waves onto the longitudinal surface of a cylinder

In this example, the target profile consists of the target 2D image of Fig. 2(b) projected onto the longitudinal cylindrical surface of the source-receiving system of Fig. 1(d), parameterized accordingly to Table 1. We modulate this target profile  $\Phi_T$  with a phase front  $\exp(iQz_r)$  with  $Q = 0.95k$  and compute its corresponding source function  $\Psi_T$  using the first 800 well-coupled modes. Fig S12(a) shows the intensity of both the target and the required source function. The simulated and reconstructed (measured) resulting waves are shown in Figs S12(b) and (c), from left to right, within a volume containing the receiving space, within the longitudinal cylindrical surface as a function of the azimuth angle  $\phi_r = \text{atan}(y_r/x_r)$  and the longitudinal distance  $z_r$ , and at the mid transverse plane of the cylinder ( $z_r = Z_r/2$ ). Measured dimensions are indicated in red in Fig. S12(c). Notice that our wavefront shaping method based on communication modes, besides providing a reconstructed profile with high intensity uniformity and contrast within the receiving curved surface, leads to a light wave with dark intensity along the optical axis over the entire longitudinal distance of the cylinder. This feature is a direct consequence from the maximization property of the communication modes (Supplementary Note 1) that guarantees that the resulting wave, delivered by the source plane onto the receiving surface, is the optimum one connecting these two spaces, with no undesired intensity away from the receiving surface.

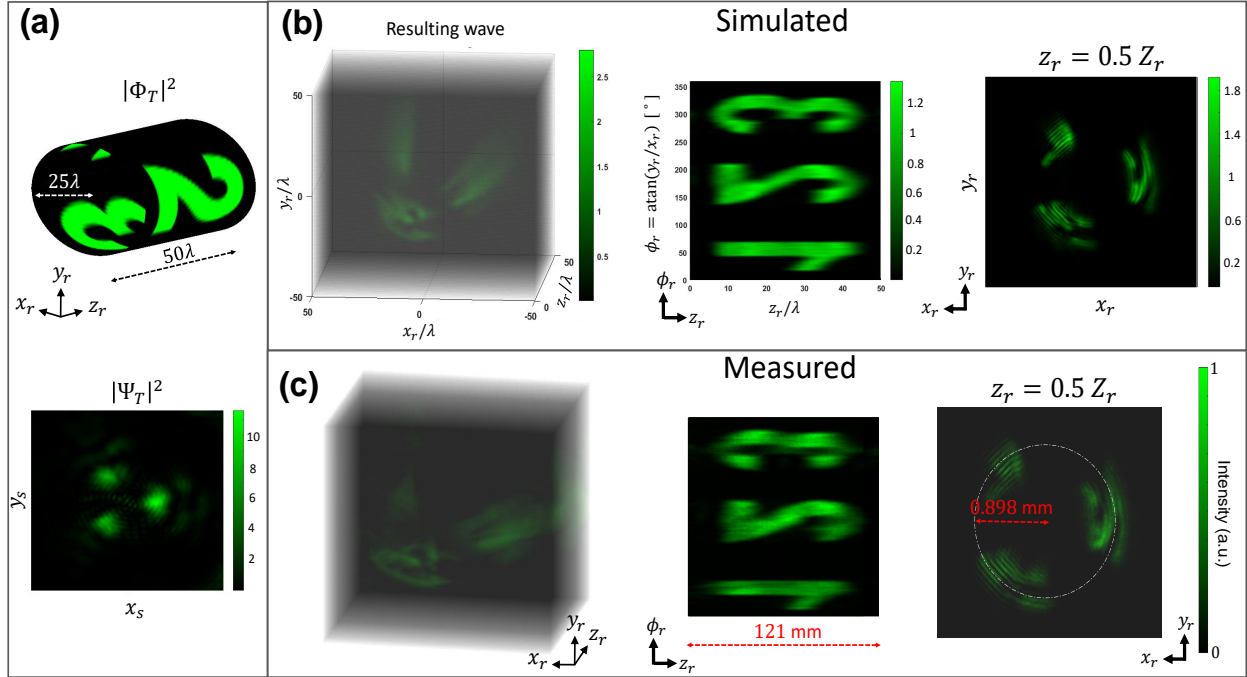


**Figure S12: Structured light field over the longitudinal surface of a cylinder using communication modes** The source and receiving configuration is the one shown in Fig. 1(d) in the main text, parameterized as listed on Table 1. **(a)** Target intensity distribution  $|\Phi_T|^2$  consists of the grayscale amplitude profile of 2D image of Fig. 2(b) projected onto the receiving cylindrical surface. Its required source function  $|\Psi_T|^2$  is computed using the first 800 well-coupled modes. **(b)** From left to right: simulated resulting wave over a volume containing the receiving space, over the lateral cylindrical surface (described in terms of its azimuth angle and the longitudinal coordinate  $z_r$ ) and at the mid transverse plane of the receiving space. **(c)** Optical reconstruction of the resulting wave using a phase-only SLM. This measured wave has a longitudinal distance of  $Z_r = 121$  mm and is projected onto the longitudinal surface of a cylinder with radius  $R_r = 0.898$  mm.

## Supplementary References

1. Miller, D. A. B. Waves, modes, communications, and optics: a tutorial. *Adv. Opt. Photon.* **11**, 679–825 (2019).
2. Miller, D. A. B. Spatial channels for communicating with waves between volumes. *Opt. Lett.* **23**, 1645–1647 (1998).
3. Miller, D. A. B. An introduction to functional analysis for science and engineering (2019). URL <https://arxiv.org/abs/1904.02539>. 1904.02539.
4. Porter, D. & Stirling, D. *Integral Equations: A Practical Treatment, from Spectral Theory to Applications*. Cambridge Texts in Applied Mathematics (Cambridge University Press, 1990).
5. Miller, D. A. B., Kuang, Z. & Miller, O. D. Tunneling escape of waves (2023). URL <https://arxiv.org/abs/2311.02744>. 2311.02744.
6. Forbes, A., Dudley, A. & McLaren, M. Creation and detection of optical modes with spatial light modulators. *Adv. Opt. Photon.* **8**, 200–227 (2016).
7. Rosales-Guzmán, C., Forbes, A. & of Photo-Optical Instrumentation Engineers, S. *How to Shape Light with Spatial Light Modulators*. SPIE. Spotlight (SPIE Press, 2017).
8. Arrizón, V., Ruiz, U., Carrada, R. & González, L. A. Pixelated phase computer holograms for the accurate encoding of scalar complex fields. *J. Opt. Soc. Am. A* **24**, 3500–3507 (2007).
9. Zamboni-Rached, M., Lourenço-Vittorino, G. d. A., Viana de Sousa, T. *et al.* Mathematical description of a Frozen Wave beam after passing through a pair of convex lenses with different focal distance. *arXiv e-prints* arXiv:1907.08202 (2019). 1907.08202.